The Thesis Committee for Scott David Drews
Certifies that this is the approved version of the following thesis:

Direct Numerical Simulations of Flow Past Quasi-Random Distributed Roughness

APPROVED BY
SUPERVISING COMMITTEE:

Supervisor: _____
David Goldstein

_____
Venkatramanan Raman

Direct Numerical Simulations of Flow Past Quasi-Random Distributed Roughness

by

Scott David Drews, B.S. As.E.

Thesis

Presented to the Faculty of the Graduate School of

The University of Texas at Austin

in Partial Fulfillment

of the Requirements

for the Degree of

Master of Science in Aerospace Engineering

The University of Texas at Austin

May 2012

Dedication

This work is dedicated to my family, Mike, Kathy, Kristen, and Marie.

Acknowledgements

I would like to thank the U.S. Air Force Office of Scientific Research, Texas Advanced Computing Center, and the Cockrell School of Engineering for their support. I also thank David Goldstein, Robert Downs, Ed White, and Nick Denissen for their insight.

Abstract

Direct Numerical Simulations of Flow Past Quasi-Random Distributed Roughness

Scott David Drews, M.S.E.

The University of Texas at Austin, 2012

Supervisor: David B Goldstein

Flow about a periodic array of quasi-random distributed roughness is examined using an immersed boundary spectral method. Verification of the code used in the simulations is obtained by comparing solutions to LDA wake survey and flow visualization experiments for a periodic array of cylinders at a roughness height-based Reynolds number of 202 and a diameter to spanwise spacing d/λ of 1/3. Direct comparisons for the quasi-random distributed roughness are made with experiments at roughness height-based Reynolds numbers of 164, 227, and 301. Near-field details are investigated to explore their effects upon transition. Vortices formed as the flow moves over the roughness patch create three distinct velocity deficit regions which persist far downstream. Simulated streamwise velocity contours show good agreement with experiments. Additional geometries are simulated to determine the effects of individual components of the full roughness geometry on near-field flow structures. It was found that the tallest regions of roughness determine the overall wake profile.

Table of Contents

Nomenclature

U_∞	= freestream velocity
U, V, W	= streamwise, wall-normal, and spanwise velocities
	= velocity vector
	= forcing vector used in immersed boundary technique
	= desired velocity
α, β	= constants used in immersed boundary technique
k	= maximum roughness height
d	= diameter of cylinder
Re_k	= roughness based Reynolds number, $U(k)k/\nu$
Re_x	= Reynolds number based on distance from plate leading edge, $U_\infty x/\nu$
Re'	= unit Reynolds number, U_∞/ν
Re_δ	= Reynolds number based on boundary layer thickness, $U_\infty\delta/\nu$
ν	= kinematic viscosity
x, y, z	= streamwise, wall-normal, and spanwise coordinates
$\omega_x, \omega_y, \omega_z$	= streamwise, wall-normal, and spanwise vorticity
η	= wall normal Blasius coordinate, y/δ
λ	= spanwise roughness element spacing (32 mm)
$\bar{U}(\eta)$	= Blasius profile velocity
U'_{rms}	= root mean square disturbance velocity
$U'_{\lambda/m}$	= disturbance velocity for spanwise mode m
u'_{rms}	= time varying root mean square disturbance velocity
E_{rms}	= total disturbance energy
$E_{\lambda/m}$	= disturbance energy for spanwise mode m
δ^*	= displacement thickness,
θ	= momentum thickness,
H	= shape factor, δ^*/θ
δ	= boundary layer thickness, $\delta^*/1.7208$
$\boldsymbol{u}$	= velocity gradient tensor
$\boldsymbol{S},\boldsymbol{\Omega}$	= symmetric and antisymmetric parts of $\boldsymbol{u}$
λ_2	= second largest negative eigenvalue of the symmetric tensor $\boldsymbol{S}^2+\boldsymbol{\Omega}^2$
$A_{n,m}$	= amplitude coefficients for the roughness surface
M	= spanwise dimensions of amplitude and phase coefficient arrays
N	= streamwise dimensions of amplitude and phase coefficient arrays
$h(x,z)$	= roughness height relative to the plate surface
$\varphi_{n,m}$	= phase coefficients for the roughness surface

I. INTRODUCTION

Transition of boundary layer flow from a laminar to turbulent state is one of the fundamental subjects in fluid mechanics. The transition to turbulence creates an increase in shear stress and heat transfer, leading to an often undesirable rise in drag and surface heating. However, accurately predicting when, where, and how transition will take place proves to be difficult. If one could better understand the transition phenomenon, intelligent methods to delay and potentially prevent transition may be developed.

Often, transition occurs due to small perturbations near the wall. These small perturbations generate initial conditions for bypass transition associated with stationary transient disturbances.[1] The transition process starts with the receptivity stage in which small surface disturbances perturb a laminar flow. These perturbations grow as the flow continues downstream, leading to a transition to turbulence. Preventing disturbances from growing beyond the receptivity region could enable a transition control approach to maintain a laminar boundary layer.

Boundary layer transition that occurs over surfaces with distributed roughness is the norm rather than the exception in aerodynamics. In the laboratory and in pristine external flow configurations, transition occurs through modal growth of Tollmien–Schlichting (TS) waves and their eventual breakdown to three dimensional disturbances. However, in many practical applications over, say, a weather-roughened wing or in a noisy turbine cascade, other mechanisms "bypass" the modal mechanisms and lead to transition at Reynolds numbers subcritical to modal disturbance growth. Subcritical growth arises from the continuous spectrum modes of the Orr–Sommerfeld (OS) equation. Surface roughness and freestream turbulence excite these decaying modes whose nonorthogonality leads to a streamwise region of transient algebraic growth

upstream of the TS neutral curve. This phenomenon is now thought to explain many bypass transition scenarios.[1]

Recent Efforts

Transient growth studies by Reshotko and Tumin[2] have motivated studies of transition induced by cylindrical roughness elements by Rizzetta and Visbal,[3] Ergin and White,[4] Stephani and Goldstein,[5] and Doolittle.[6] Downs et al.[7] has recently investigated transient growth downstream of quasi-random distributed roughness patches, which is much more representative of real world aerodynamics than discrete roughness elements.

Optimal disturbances, disturbances that produce the largest algebraic growth over a specified streamwise extent, have been investigated in studies by Andersson et al.[9] and Tumin and Reshotko.[10] These studies focused on optimal disturbances present in parallel-flow boundary layers. Tumin and Reshotko[10] extended their analysis to varying pressure gradients to show that a favorable pressure gradient decreases the growth rate of the optimal disturbances. A limitation of transient growth theory may be due to inadequate representation of the near-field details,[8] thus transient growth studies of flow past roughness may require a more complete representation of near-field details. Such flows may need to be solved computationally as experiments are often limited by physical constraints.

Surface roughness produces suboptimal initial disturbances[8] (as opposed to optimal disturbances). The experiments of White,[11] Ergin and White,[4] and Downs et al.[7] show that roughness induced transients do not behave according to optimal theory prediction (a further discussion on the respective results is seen in chapter III). Therefore, an analytic solution for instability growth due to surface roughness does not

exist and extensive studies into the transients created by near-field flow structures are performed.

Many studies in transition focus on flow past sand-grain and other more realistic roughness. Early studies in turbulent flow over sand grain roughness by Nikuradse[12] were instrumental in not only determining a height scale for flow over moderately realistic roughness, but also the effect of maximum roughness height on the turbulent downstream wake. Laminar to turbulent transition studies by von Doenhoff and Elmer[13] and Dassler et al.[14] have shown that sand-grain roughness below a critical height based Reynolds number, Re_k, does not create disturbances that promote a transition to turbulence. Von Doenhoff and Elmer also found a flow will transition to a turbulent state at the same location downstream regardless of the streamwise length of the roughness provided the peak roughness height remains the same.[13] This allows for comparisons to be made between experiments as long as the maximum roughness heights are the same. Recent efforts by Downs et al.[7] have investigated transient growth downstream of quasi-random distributed roughness elements. Unlike sand grain or sandpaper roughness, the quasi-random distributed roughness is designed to excite only specified flow modes to better understand their effect on the transition process. This allows one to have much more control in creating the roughness elements.

The findings of these prior studies indicate that the most important factor in determining if the disturbances introduced by realistic roughness will lead to a transition to turbulence is the maximum height of the roughness relative to the boundary layer thickness. This is a substantial finding because of the difficulty in creating two identical roughness patches and matching all flow parameters for two different experiments. Moreover, a flow will transition to turbulence with little regard to the roughness shape

and streamwise extent of the roughness region if the peaks of the roughness are above a critical height-based Reynolds number of around 250.

II. COMPUTATIONAL APPROACH

The computational method utilized in this thesis was developed by Goldstein et al.[15] who combined the spectral code described by Handler et al.[16] with an immersed boundary technique. This combination allows for the simulation of laminar or turbulent flows over complex stationary or moving solid surfaces. Spatial derivatives are computed using a Fourier series in the streamwise and spanwise directions and a Chebyshev polynomial in the wall normal direction, allowing for transfer to and from spectral space. The use of Fourier and Chebyshev expansions allows for low error solutions to the Navier-Stokes equations. To achieve these expansions, a 3/2 de-aliasing grid is used in the Fourier directions and a cosine grid in the Chebyshev direction.[16,17] The cosine grid creates regions of closely spaced grid points near the wall boundaries. The code used is both spanwise and streamwise periodic; flow that leaves the left side of the domain is inserted on the right side and vice versa. Also, fluid that leaves the streamwise extent of the domain flows into a buffer zone where it is reformed back into a Blasius flow. A semi-implicit time step is used wherein the solution of the viscous terms is achieved using a Crank-Nicholson method and the nonlinear terms with an Adams-Bashforth method.[18]

The immersed boundary technique introduces a localized body force field into the incompressible Navier-Stokes equations. This force field is made to adapt to the flow at a particular grid point and bring it to the desired velocity. This adaptation is based on a two-parameter control scheme which provides feedback based on the flow's current velocity and the velocity history at that point. The control scheme equation at a grid point of the immersed boundary is:

where (x,t) is the current velocity vector, $_{des}$ is the desired velocity vector, α and β are spatially varying negative numbers which are constant in time, and (x,t) is the body force vector applied in the region of that grid point. This approach is particularly well suited to modeling the distributed roughness geometry described below. See Goldstein et al.[15] for a more detailed explanation of the immersed boundary method.

A. Simulation of a Blasius Boundary Layer

The code used is a channel flow code that was modified to simulate boundary layer flow. A buffer zone and a suction wall were added to create the desired inlet Blasius profile. The buffer zone incorporates the same control scheme as for an immersed solid surface, but with spatially varying α and β. See Strand[19] for more information on the buffer zone.

A suction wall is needed at the top of the domain to create the proper vertical velocity above a boundary layer. Without the suction wall, the no through flow boundary condition at the top of the channel constrains the flow creating a favorable pressure gradient and preventing the Blasius profile from growing properly. An immersed boundary is used to create this suction wall by applying the Blasius streamwise and vertical velocities on that wall. Figure 1 shows a schematic of the computational domain of Strand[19], which is used in the present work as well. The top image in figure 1 shows four distinct regions in the domain. Regions I and II are in the buffer zone where the Blasius flow is created. Regions III and IV are outside of the buffer zone with region IV representing the area of interest and region III representing flow above the suction wall.

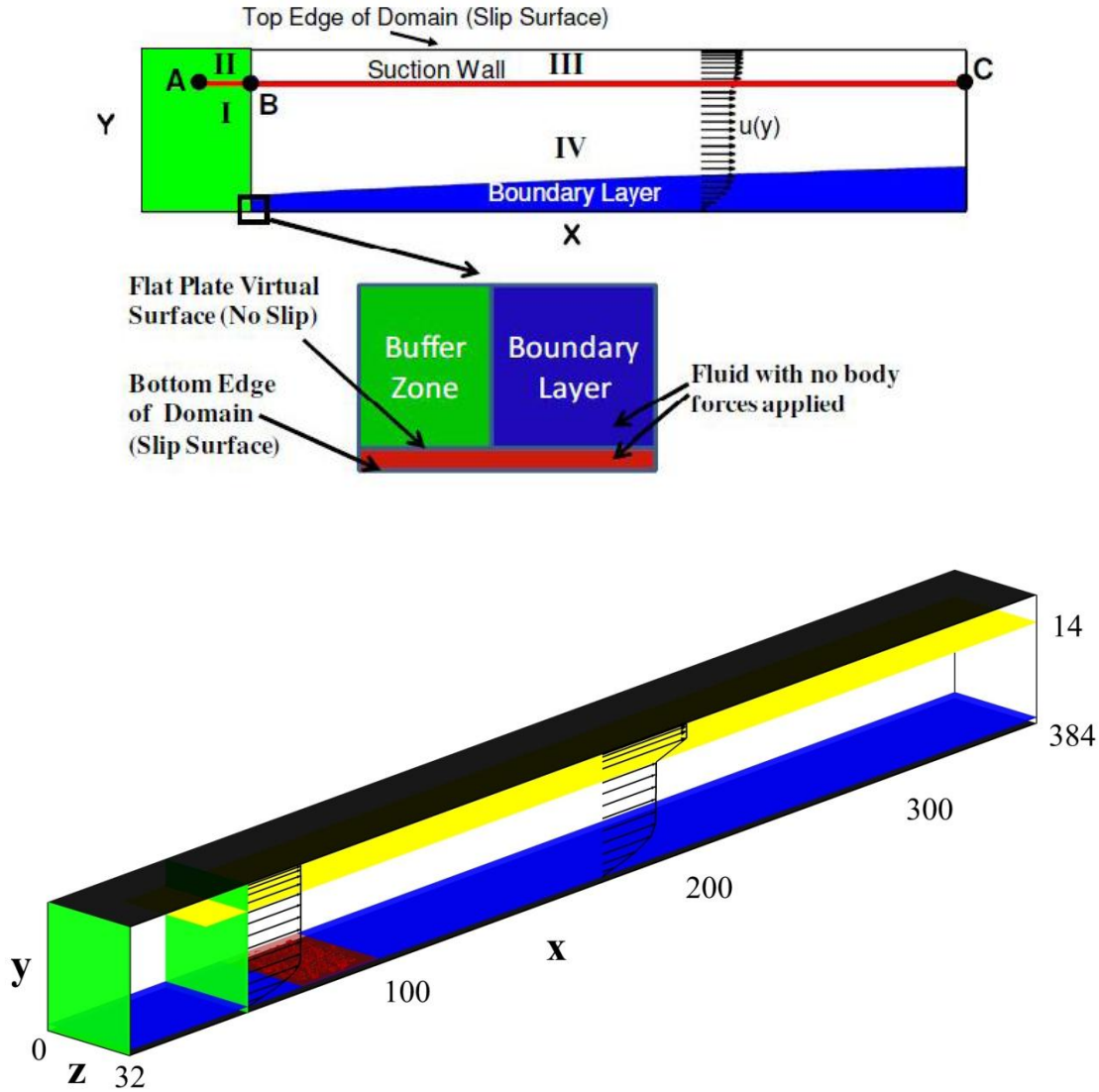

Figure 1: On top is a schematic of computational domain with buffer zone and suction wall employed to model a Blasius boundary layer. Image shows the entire domain, and is stretched in the y-direction but is otherwise to scale. Detail shows the virtual plate, and the small area of fluid beneath it. Region IV is the region of interest in which the roughness element is placed. On the bottom is a perspective view showing the placement of a red roughness element in this domain.

In previous work[5,6] it was thought that only the correct vertical (V) velocity had to be applied at the suction wall in order to obtain a Blasius velocity profile and zero pressure gradient in region IV. However, we found that there were some minor inconsistencies in the profile and an apparent weak adverse pressure gradient. In an effort to remove this pressure gradient, streamwise (U) velocity forcing was thus coupled with the imposed vertical velocity at the suction wall. This reduces a slight adverse pressure gradient created due to the lower solid wall (blue in figure 16) being located higher than in the previous simulations of Doolittle[6] and Stephani and Goldstein.[5] Figure 2 shows the effect of streamwise velocity forcing at the suction wall on the Blasius profile. Adding forcing in the streamwise direction changes the original shape factor, H (ratio of displacement thickness to momentum thickness), of 2.677 to 2.608, which falls in the acceptable range (H=2.591±0.02) for studying transition in a Blasius flow.[20] The integrals for the displacement thickness and momentum thickness are calculated over the range of $0 \leq \eta \leq 8.5$ to ensure that the entire boundary layer is included (η=6 is end of boundary layer) and that the suction wall (starting at $\eta \sim 14$) is not included.

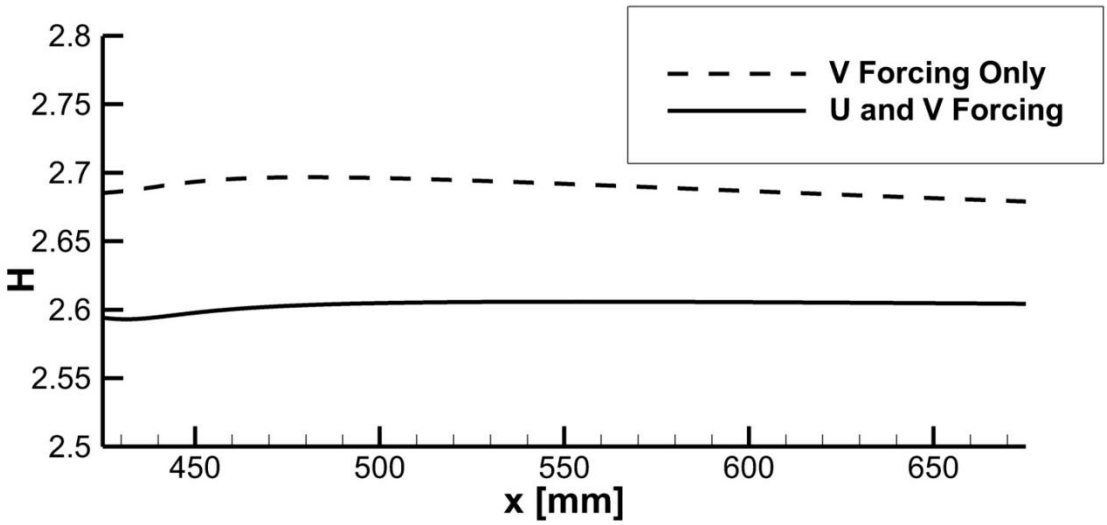

Figure 2: Shape factor comparison of nominally Blasius flow for a suction wall enforcing only vertical velocity to a suction wall enforcing both vertical and streamwise velocities.

B. Computational Details

The computational domain represents a physical region of streamwise length x = 384 mm, spanwise width z = 32 mm, and wall normal height y = 19.5 mm. for the quasi-random distributed roughness simulations. The typical numbers of grid points used in simulations are N_x = 1536, N_z = 192, and N_y = 192. The chosen number of grid points and physical dimensions creates minimal error in recreating the roughness patches of Downs et al.[7] Before deciding upon the final physical length in the wall normal direction, several physical lengths are examined and it is found that decreasing the physical length leads to larger errors near the tops of the roughness, while increasing the physical length significantly decreases the number of grid points near the virtual flat plate. Transformation to and from Fourier space using the de-aliasing grid gives physical

resolutions of 0.25 mm and 0.167 mm in the streamwise and spanwise directions, respectively. Variation in the wall normal cosine grid spacing produces spacings of 1.401 mm near the centerline down to 0.0147 mm near the solid roughness elements. A time step of 1.5 x 10^{-6} seconds is used as in prior applications of the code[5,6,20] and validated by CFL stability during initial phases of the simulation while temporal gradients are largest. Computations are performed on twelve processors of the Texas Advanced Computing Center Dell Xeon System.

For direct comparison to the cylinder results of Rizetta and Visbal,[3] Ergin and White,[4] Stephani and Goldstein,[5] and Doolittle[6] the buffer zone is used to produce an initial Blasius profile at a physical distance of 257 mm from a flat plate leading edge, corresponding to an Re_k of 205 and an Re_x of approximately 225,000. The current simulation models a periodic array of cylinders with a spanwise center to center spacing, λ, of 19 mm located a distance of 300 mm from the leading edge. A nominal freestream velocity of U_∞=12.2 m/s is used with a code Reynolds number Re_c of 62,623 to maintain consistency with previous studies.

For direct comparison to the random roughness experiments of Downs et al.[7] in air, the buffer zone is used to produce an initial Blasius profile at a physical distance of 338, 339, and 389 mm from a flat plate leading edge for the three simulated values of Re_k of 164, 227, and 301. In this manner we simulate a roughness patch at x_k = 434 mm from the leading edge with a 32 mm spanwise center-to-center spacing, λ, between adjacent roughness patches, matching the setup of Downs et al.[7] directly. Nominal freestream velocities of U_∞=7.5, 9.3, and 11.5 m/s are used with a code Reynolds number Re_c of 55,161 to again maintain consistency with experiments. These parameters give Re_x values of roughly 150,000, 200,000, and 250,000, well below the limit of T-S wave instability.

C. Roughness Elements

The roughness elements are created using the immersed boundary technique described earlier. For roughness elements with no slip surfaces, the body forces created bring all three velocity components effectively to zero on the frozen grid points. Since the no slip condition is enforced only at grid nodes, a high resolution grid is used to minimize jagged edges created by the discrete nature of the grid. Two types of roughness are examined, cylinders and random distributed roughness.

The cylinders in the DNS[5,6] have a height of 0.7304 mm and diameter of 6.35 mm to match those used in experiments performed by Ergin and White.[4] Cylinders were chosen for the validation portion of the study because of the symmetric flow in the wake and availability of experiments and alternate simulations to compare results. One issue encountered when creating the cylinders was the stairstep edges created when representing a rounded surface on a Cartesian mesh[5,6]. With the original grid spacing of 0.195 x 0.098 mm in the streamwise and spanwise directions, respectively, the cylinder had under-resolved edges. To solve this, the number of grid points in the spanwise direction was doubled (from 193 to 385) and the physical domain length in the streamwise direction was halved, creating a 4x increase in resolution. Figure 3 shows the cylinder as represented by the Cartesian mesh for both the lower and higher resolution simulations.

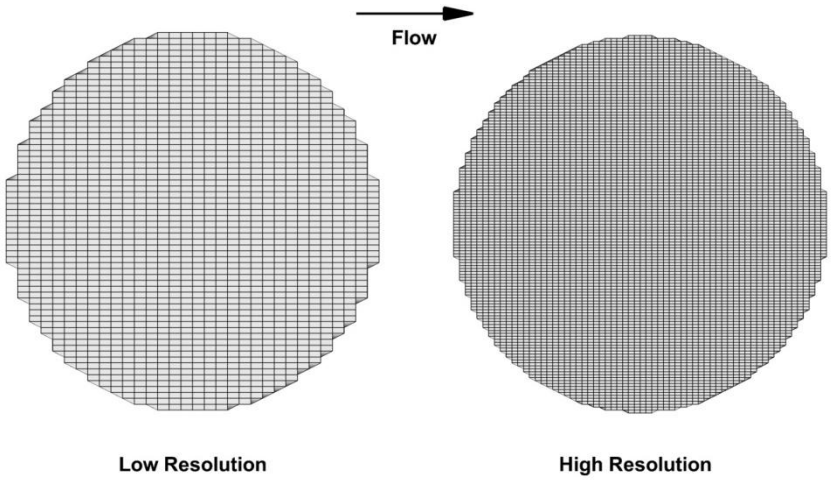

Figure 3: Comparison of low resolution (left) and high resolution (right) cylinders. High resolution cylinder has twice the number of spanwise and streamwise gridpoints that define the cylinder.

The quasi-random distributed roughness patches used by Downs et al.[7] were created by selecting random amplitudes and phases of Fourier coefficients to numerically generate a roughness element using

and manufactured using a rapid-prototyping machine. There are several advantages to this approach. Since the exact height is known at each x,z location, it can easily be recreated for use in other experiments or DNS. Another advantage is the spanwise periodicity used in experiments. A phase-locked average can be calculated to reduce noise. And the periodic nature matches DNS boundary conditions. A third advantage is the ability to include features to simplify experiments. Downs et al.[7] used flat regions at the wall between the roughness patches to aid the hotwire in locating the wall location.

The flat regions were created by multiplying the original amplitude coefficients by a smoothing envelope function in the streamwise and spanwise dimensions. Figure 4 shows the pre-envelope and post-envelope amplitude coefficients.

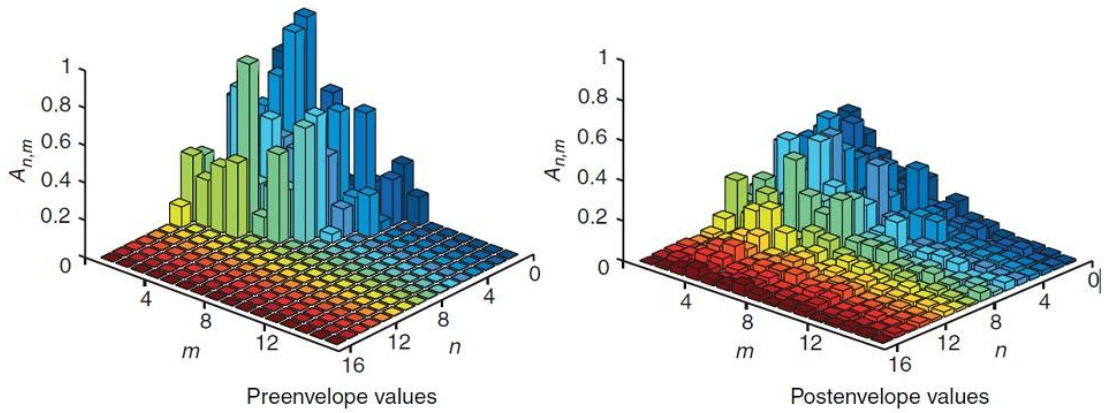

Figure 4: Pre-envelope and post-envelope amplitude coefficients used in creating roughness patch. Picture taken from Downs et al.[7]

The specified amplitude of the experimental roughness is -0.9 to +1.0 mm with a resolution (set by the rapid-prototyping machine) of 0.1 mm. The chosen flow velocities of U_∞7.5, 9.3, and 11.5 m/s correspond to Re_k values in experiments of 164, 227, and 301. Additionally, all three height based Reynolds numbers have an Re_δ above the critical value of 302, allowing for potential T-S wave growth downstream of the roughness element.

III. CODE VERIFICATION

Validation of the DNS used by Doolittle[6] and in current simulations is necessary to show the DNS provides realistic results. First, DNS results for flow around discrete cylindrical roughness elements are compared to previous (and current) experimental and computational results. This is accomplished via two distinct approaches: a comparison of roughness wake velocity contours and comparison of water channel flow visualization of near-field structures to those seen in our DNS. Matching both criteria provides confidence that the code used in previous and current DNS accurately represents the near-field details of flow past roughness elements.

Second, the geometry of the simulated quasi-random distributed roughness patch is compared to the actual quasi-random distributed roughness patch used in experiments.[7] This entails both a qualitative comparison of the overall shapes of the two roughness patches, as well as a quantitative comparison of the height difference between the two roughness patches.

A. Water Channel Experiments for Flow Over Discrete Cylinders

To compare results from experiments of Ergin and White[4] and Rizzetta and Visbal[3] and simulations of Doolittle,[6] flow visualization and LDA wake survey experiments were conducted on a 13.5 mm diameter, 1.38 mm tall cylindrical roughness element in a closed circuit water channel. The experiments were run at an Re_k of 196, matching closely the Re_k of 202 used in the experiments of Ergin and White.[4] The tests were conducted at a freestream velocity of 0.37 m/s on a 1 meter long flat plate in the 0.381 m x 0.508 m x 1.542 m test section. The plate had a 4:1 elliptical leading edge and was transparent for suitable flow visualization. A Dantec FlowLite 2D LDA was used to

obtain U velocity contour 2D slices downstream of the cylindrical roughness element with fine and coarse grid resolutions of 0.075 mm by 0.2 mm and 0.5 mm by 1 mm for the wall normal and spanwise directions. The coarse grid was used to capture data outside of the main wake structure while the fine grid was used to capture data in the main wake. This division was created to shorten the run times associated with using the fine mesh over the entire domain. The fine grid is superimposed on top of the coarse grid in the results presented later in figure 8. The LDA operates at a wavelength of 632 nm and a beam expander with a focal length of 310 mm was used to create an acquisition volume of 0.105 mm x 0.105 mm x 0.408 mm, a higher spanwise resolution than available with the hotwire in Ergin and White.[4] The grid spacing of experiments in Ergin and White[4] was 0.157d by 0.904k for the spanwise and wall normal respective directions, while the grid spacing of LDA results were 0.286d by 0.362k and 0.015d by 0.054k for the coarse and fine grids, respectively. Our experimental roughness height to diameter ratio, k/d, and Reynolds numbers used, Re_x and Re_k, matched those of prior and our subsequent DNS.[5,6,21]

Flow visualization was done using dye ports on the bottom of the flat plate holding the cylindrical roughness element. Water soluble food coloring was injected upstream of the roughness elements to examine flow structures found in the DNS detailed by Doolittle[6] and in a more refined way in this document. A schematic of the water channel setup is shown in figure 5.

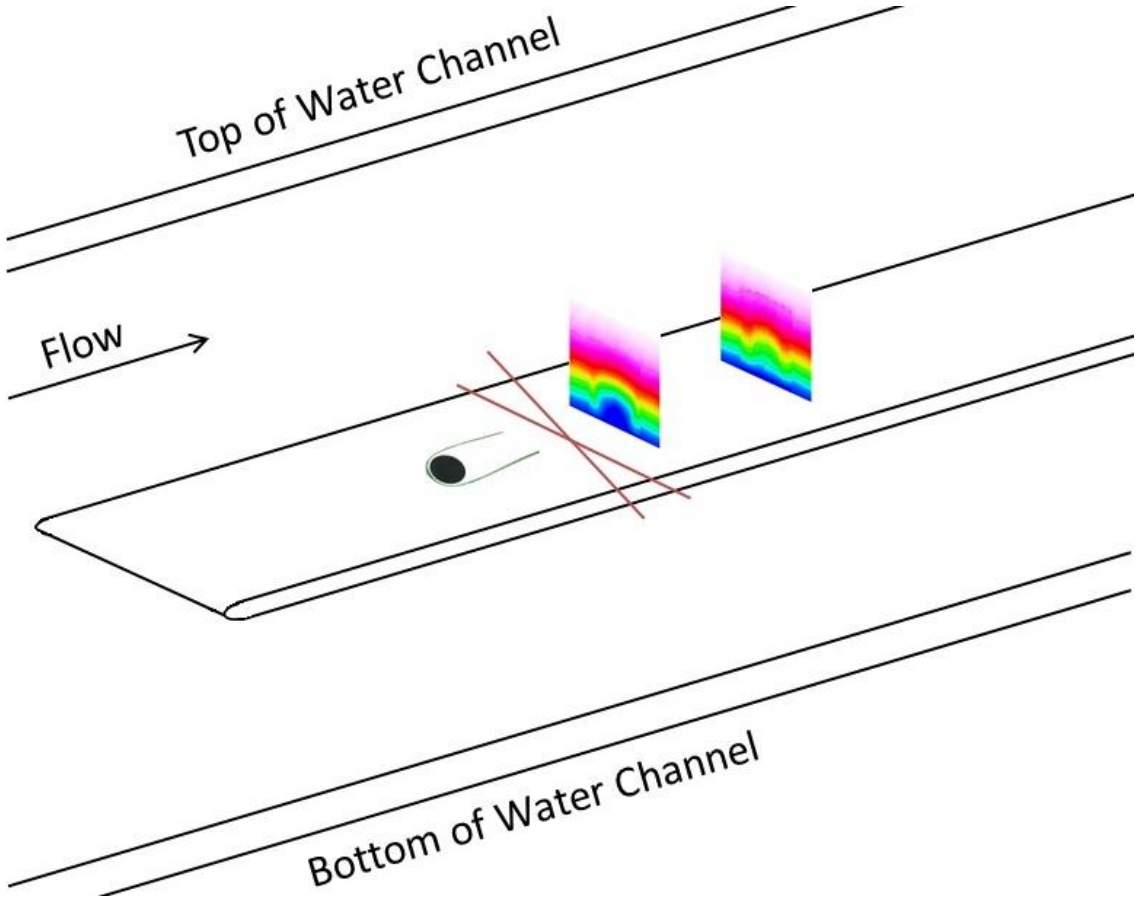

Figure 5: Schematic of water channel setup. Green collar vortex represents flow visualization, red lines represent LDA beams, and velocity contour slice represents LDA data. Note: not to scale.

B. Flow Visualization

We first examine the flow over cylindrical roughness elements with an eye toward confirming that the current DNS can accurately reproduce detailed flow structures. DNS results[6] show three distinct collar vortices in the flow (figure 6). Using dye injection it is clear three collar vortices are present. Figure 7 is a comparison to DNS of photographs from the water channel showing the three vortices in different colors. Figures 7e and 7f

are created from analyzing several photographs of each single collar vortex. Due to limitations in the dye port configuration, separate dye colors cannot be injected into the individual cores simultaneously. Instead, each of the three cores is identified separately by manipulating the flow of the dye out of the bottom of the plate (figures 7b, 7c, and 7d). Once all three cores are observed independently of each other, one can photograph all three together (figure 7a). This indicates that, in the visualization process, the three collar vortices present are independent, allowing one to examine each individual core or the three as a whole. This image is then altered in Adobe Photoshop to create figure 7f. Each individual collar vortex is colored to help distinguish the three, and the overall composite image is compared side by side to the DNS.

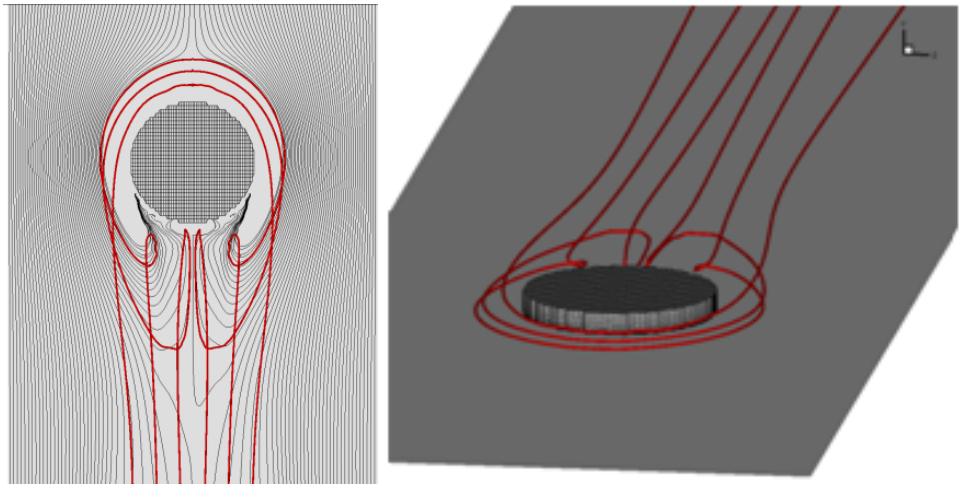

Figure 6: DNS results showing three collar vortices. Left image is top down and also shows surface streamlines; right image is a perspective view.

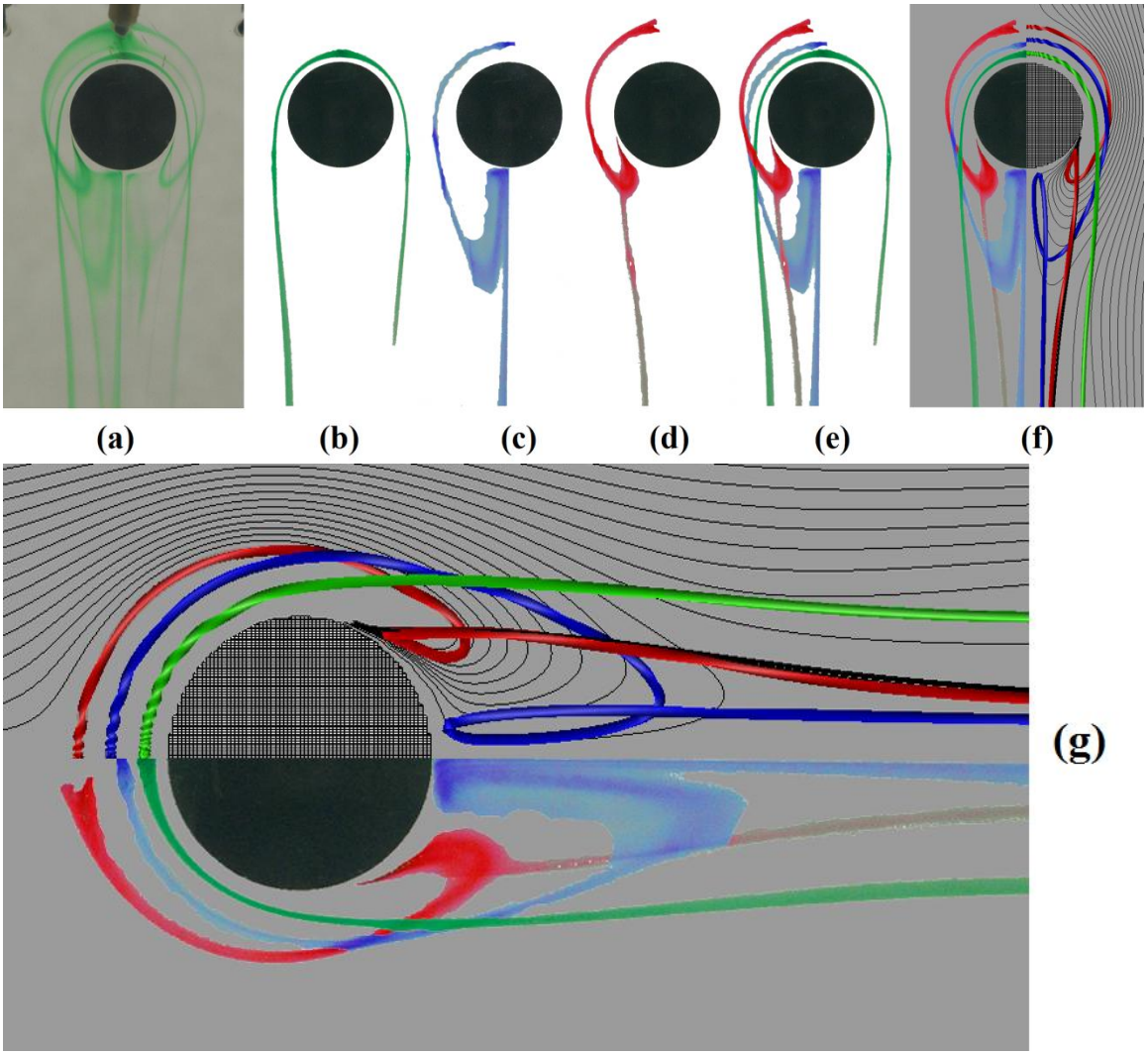

Figure 7: Top: Buildup of water channel flow visualization and comparison to DNS results. Left image (a) is original image from the water channel, right image (f) is after artistic filtering of vortices by color. Bottom: Large image of final comparison.

The bottom image of figure 7 shows excellent agreement of the *primary* (green) cores between flow visualization and DNS results. However, the results show slightly different standoff distances for the *secondary* (blue) vortex cores. This may be due to the slightly blunt leading edge of the cylinder used in DNS causing an alignment issue with

the photograph from the water channel. The turn locations of the *secondary* core downstream of the cylinders agree well as do the turn locations of the *tertiary* (red) cores.

C. LDA Results

Figure 8 shows LDA slices from the present water channel studies next to the current high resolution simulation (the cylinder being resolved by ~120 grid points), the experimental results of Ergin and White,[4] the DNS of Rizetta and Visbal,[3] the DNS results of Doolittle[6] (with the cylinder being resolved by ~60 grid points), and the DNS of Stephani and Goldstein[5] (with the cylinder also being resolved by ~60 grid points) all for an Re_k of nearly 202 (Re_x ~225,000). Data are presented for slices 3/2, 6, and 9 diameters downstream from the center of the cylinder for all but the LDA (LDA data are only for 3/2 and 6 diameters due to large amount of noise in 9 diameter LDA data).

The LDA data show a slightly steeper hump than DNS results of Rizzetta and Visbal.[3] Data from Ergin and White[4] show a similar single hump structure, but are limited by the spanwise resolution of the hotwire used. The DNS results of Doolittle[6] show a three hump structure not present in any of the other results. The three hump structure is due to a lack of resolution of the cylinder modeled in the DNS of Doolittle.[6] The low resolution created jagged or stair step edges on the trailing edge of the cylinder which affected the shape of the free shear layer being shed by the element causing it to wrinkle into four instead of two trailing near-field flow structures.

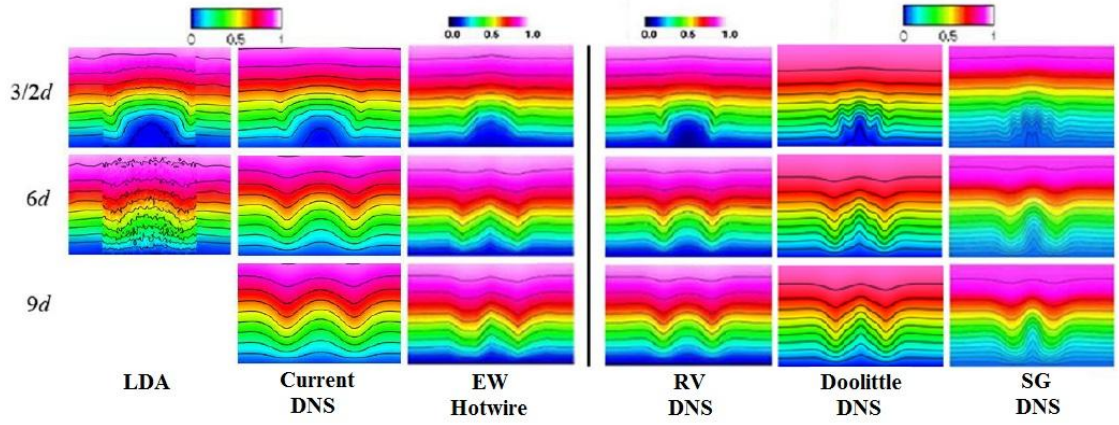

Figure 8: Comparison of streamwise velocity contours on streamwise normal slices 1.5, 6, and 9 diameters downstream of the center of the element. Left column is LDA experiments in water tunnel, second column is high resolution DNS, third column is EW hotwire experiments, fourth column is RV DNS, fifth column is Doolittle DNS, and right column is SG DNS. Note that vertical stretching is used to highlight the differences between the images.

Other than that, there appear to be no significant differences between the flow structures found in the low and high resolution simulations. The second column is a current high resolution simulation having twice as many grid points in spanwise and streamwise directions as used in the Doolittle DNS.[6] The single hump structure in the current high resolution simulation shows good agreement with the LDA experiments, experiments of Ergin and White,[4] and DNS of Rizzetta and Visbal.[3] It appears the DNS used in current work over the quasi-random distributed roughness (below) captures the near-field details over the more simple cylindrical element well. We further explore the effects of grid resolution on this flow in Doolittle et al.[21]

D. Geometry of the Quasi-Random Distributed Roughness Patch

The roughness patch used in Downs et al.[7] proves to be much easier to recreate on a Cartesian mesh than the cylinder previously simulated. The chosen number of 128 spanwise grid points (192 on the 3/2 de-aliasing grid) and a physical width of 32 mm allows for a resolution of 6 points per millimeter or Δz=0.167 mm. The selection of 1024 streamwise grid points (1536 on the 3/2 de-aliasing grid) and a physical length of 384 mm yields a resolution of 4 points per millimeter or Δx=0.25 mm. The original thought was to use a streamwise resolution of 0.167 mm, the same as the spanwise resolution. This allows for measurements to be taken up to 616 mm downstream of the flat plate leading edge. However, in order to compare results against those of Downs et al., measurements in the simulation need to be taken at least 650 mm downstream of the leading edge. Figure 9 shows the domain simulated, excluding the buffer zone. Measurements can be made up to 744 mm downstream of the flat plate leading edge.

The representation of the roughness patch itself is verified next by both qualitative and quantitative means. Before determining quantitatively how accurately the cosine grid used in simulations can reproduce the roughness patch of Downs et al.[7], the two are visually compared to make sure that the distinct regions of roughness within the patch occur in the same place. Figure 10 shows the comparison between experimental and simulated roughness patches. Larger pictures (to enhance detail) of the roughness patches used in experiments and simulations are shown in figure 12. The left image of figure 10 shows two of the five roughness patches used by Downs et al.[7] to create a periodic array. The right image shows the roughness patch used in the present simulations. Only one roughness patch is needed in simulations because the DNS code is spanwise periodic in nature.

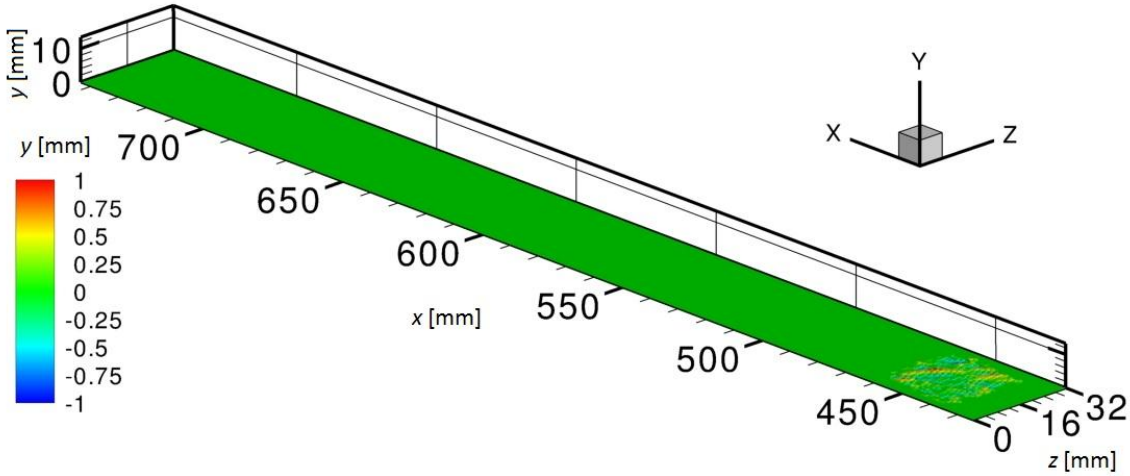

Figure 9: Streamwise and spanwise extent of domain simulated. Wall normal extent represents 13.4 mm of the total 19.5 mm. Roughness colored by wall normal height as shown on color bar. X-axis labeled at distance downstream of nominal flat plate leading edge.

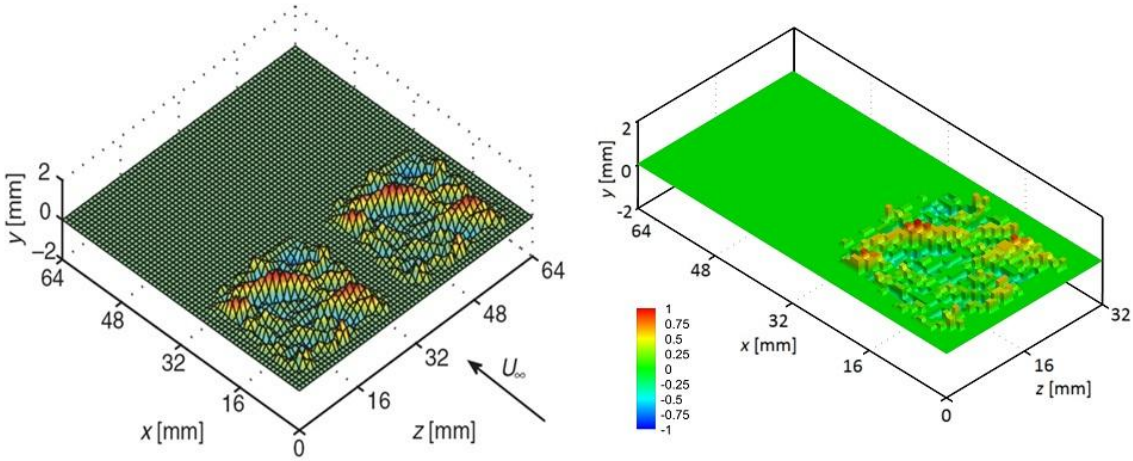

Figure 10: Comparison of roughness patches used in Downs et al.[7] (left) and DNS (right). Note: Both images stretched vertically by a factor of 4 to emphasize detail.

The height of each specified amplitude input to the rapid-prototyping machine is checked against the corresponding height in the simulated roughness patch. From this, the percent error is calculated (equation 3) and shown in figure 11. It is clear that the cosine grid used in the wall normal direction does a good job of accurately recreating the roughness patch, however it is not perfect (max error is 5.56%). This leads to a small error of approximately 10 in the Re_k values simulated compared to those used in experiments. Despite this error, the simulation with an Re_k of 237 (227 for experiments) still falls below the critical Re_k of 250 for potential unsteadiness and transition to turbulence.[4,7]

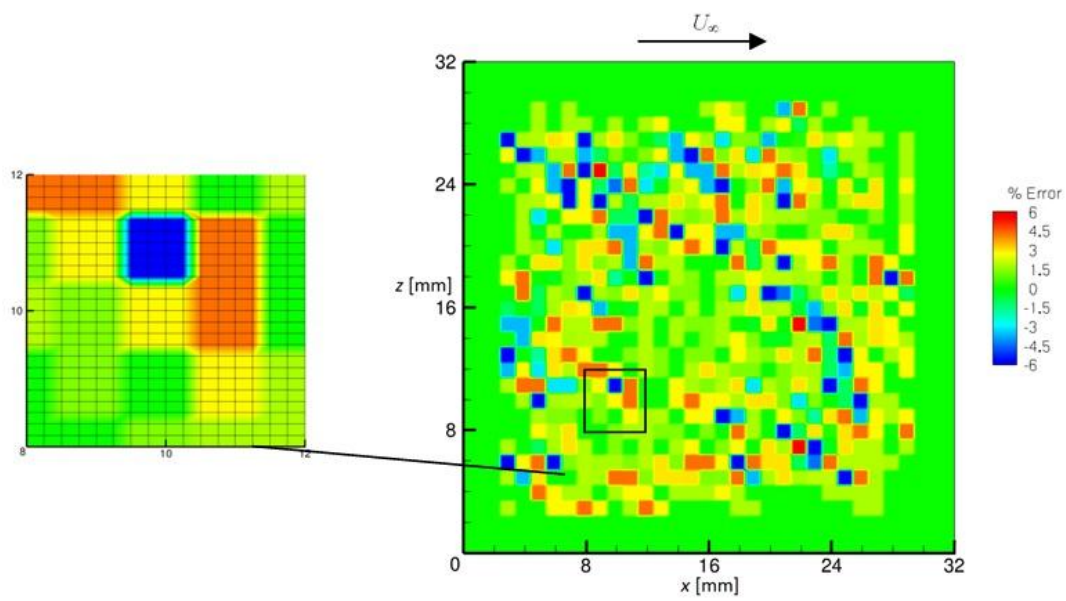

Figure 11: Percent error plot of experimental and simulated roughness patches. Detail on left shows grid resolution of 0.25 mm by 0.167 mm for streamwise and spanwise directions, respectively.

The enlarged domain images in figure 12 show a difference in the smoothness of the roughness that should be expected to lead to discrepancies between the experimental and computational results. The roughness patch used in experiments (top image of figure 12) has a much smoother appearance than the roughness patch used in simulations (bottom image of figure 12). The sharp cusps of the simulated roughness around the small scale roughness features (like stacked tiles) should cause both lateral gradients (created as the flow turns around the roughness) and the top shear layer (created as the flow moves over the top of the roughness) to develop in a different manner than in experiments. This most likely results in stronger gradients in simulations, leading to larger disturbances and more distinct wake profiles downstream of the roughness. Note: figure 12 identifies the A, B, and C regions of tallest roughness that will be referenced in subsequent sections of this thesis.

The final step in verification was ensuring the no through flow and no slip boundary conditions are satisfied over the entire roughness patch. This was performed by first measuring | | on all solid surfaces and verifying that | |<0.001 m/s, and then placing streamlines and checking that no streamlines pass through a solid surface.

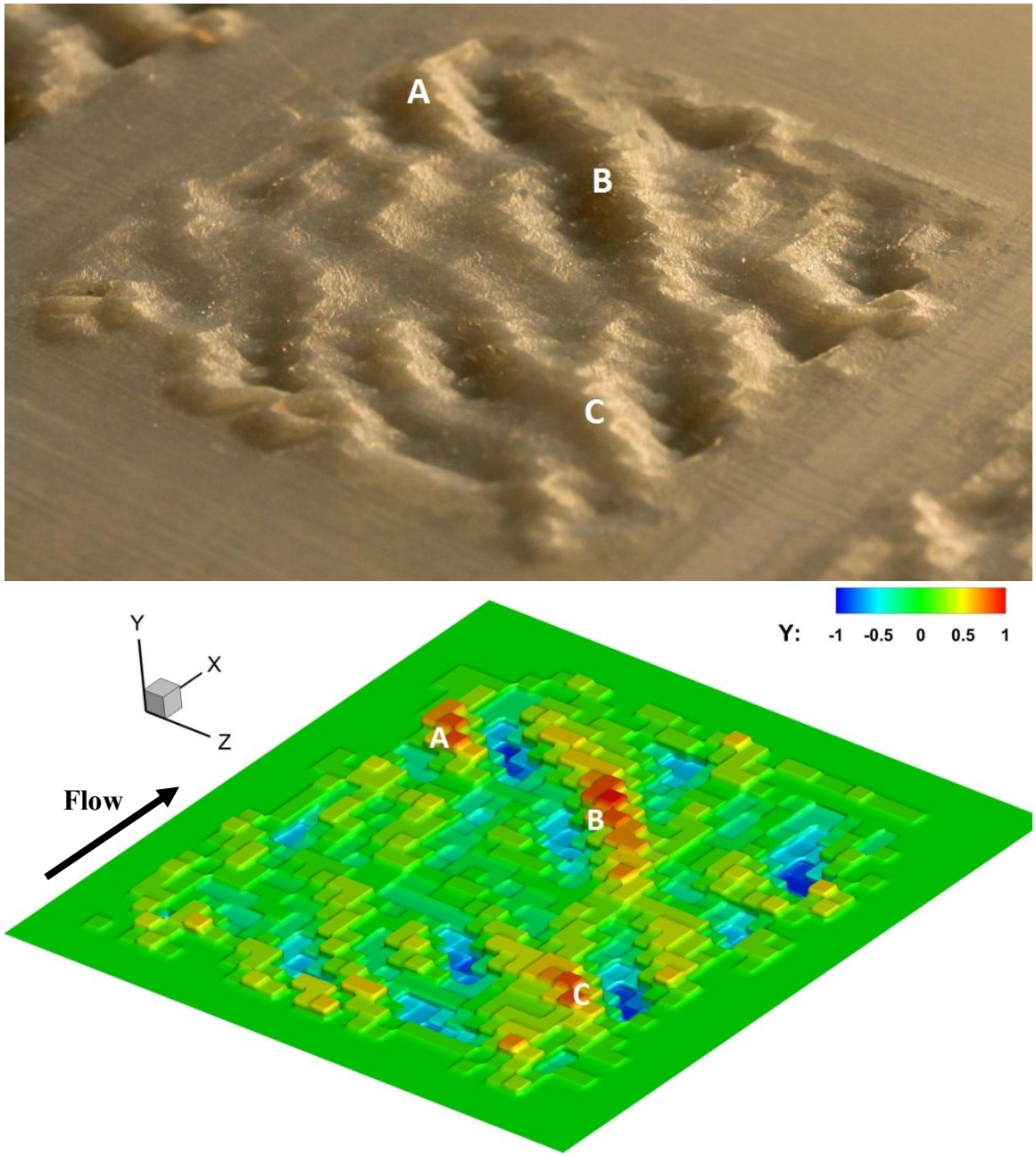

Figure 12: Detailed domain comparison between experimental and simulated roughness patches. Top image is photograph of roughness used in Downs et al.[7] and bottom image is roughness used in simulations. Note: A, B, and C regions of tallest roughness introduced and labeled.

IV. RESULTS

This chapter focuses on the results of the simulations performed for the three values of Re_k (164, 227, and 301) used in experiments of Downs et al.[7] Also presented are results of various alternate geometries to better understand the effects of individual components of the entire roughness patch on the near-field details.

A. Re_k 164

The first simulation we discuss is at a U_∞ of 7.5 m/s, corresponding to an Re_k of 164. The low height-based Reynolds number does not allow for very strong gradients to develop, and thus the overall flow is much less disturbed than in subsequent higher Re_k simulations.

The overall flowfield for Re_k 164 is shown in figure 13. The streamlines in the very near-field show a strong tendency to swirl around the vortex cores created as the flow moves over the roughness patch. These vortex cores create three distinct velocity deficit regions, centered around z=6, 14, and 23 mm (z/λ_k=-0.3, -0.05, and 0.2), respectively. Further examination of the nature of these velocity deficit regions is presented in the similar Re_k 227 results section (below). Due to the low height based Reynolds number, the initial vorticity created from the roughness patch quickly dissipates as the flow moves downstream.

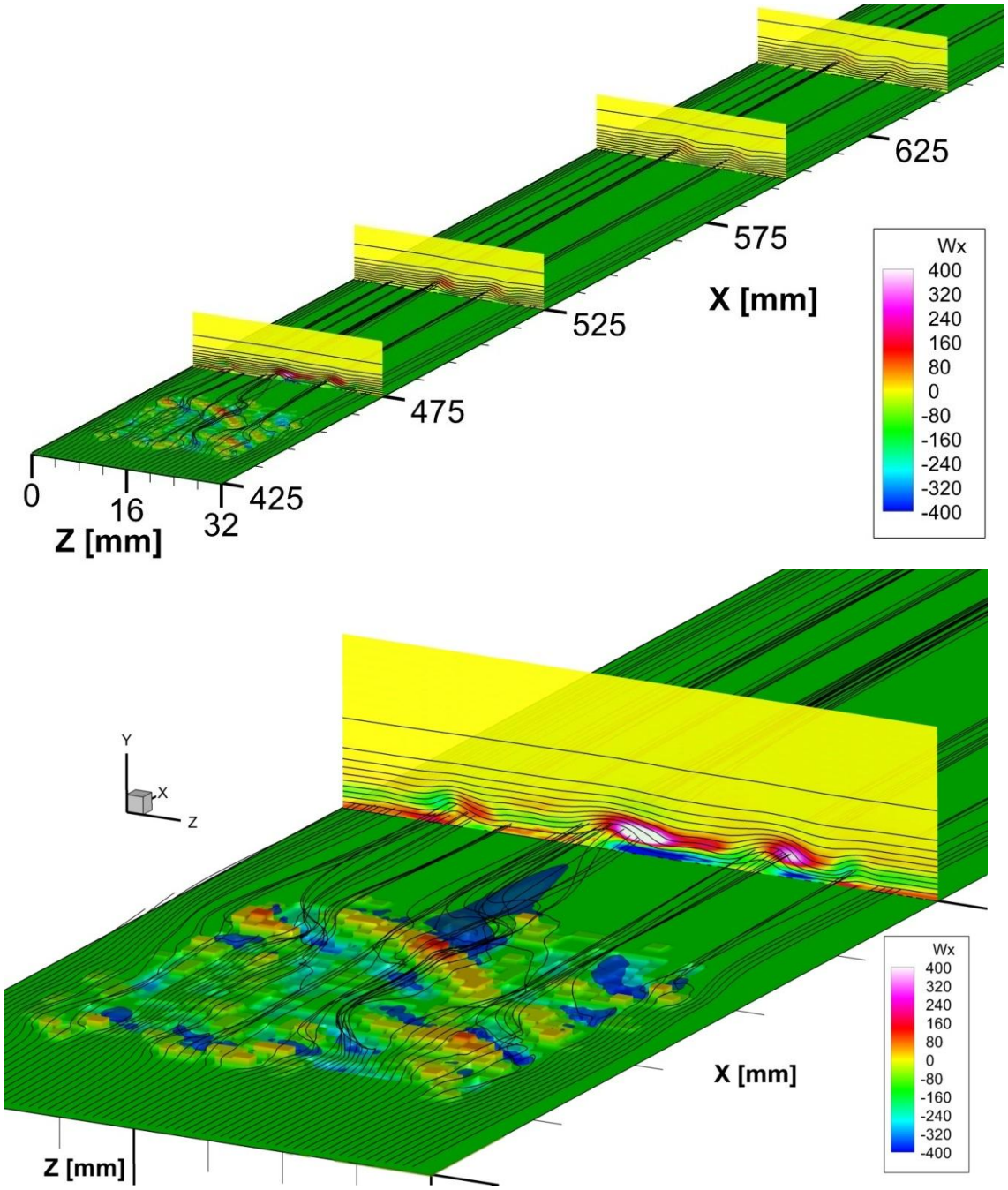

Figure 13: Top image shows overall flowfield for Re_k 164. Slices colored by ω_x with contour lines in 10% U_∞ increments. Roughness patch colored by height, streamlines at an initial height of y=0.25 mm shown in black. Bottom image shows detail of flow over the roughness patch and the x=475 mm slice. Blue iso-surface of negative U velocity shown. Other coloring is the same as in the top image.

The slices at x=475, 525, and 600 mm showing streamwise velocity are compared against those from the experiments of Downs et al.[6] in figure 14. Experimental data were collected using a single component hotwire probe, allowing for measurements of streamwise velocity only. Contour lines are in 10% U_∞ increments with coloring by U. DNS and experimental data compare well at 475 mm downstream, however, the disturbances dissipate more quickly in experiments than in DNS as the flow moves further downstream. The velocity deficit regions in the DNS reach higher into the boundary layer than in the experiments. This is most likely due to the sharp cusps present in the computational roughness previously discussed in the *Geometry of the Quasi-Random Distributed Roughness* section of chapter III. The shear layer created as the flow moves over the top of the DNS roughness does not develop in the same manner as in experiments. As discussed earlier, the results from the flow around cylinders in Doolittle[6] show a three hump structure not seen in experiments[4] due to sharp cusps and stairstep edges not allowing the shear layer to move over the trailing edge of the cylinder properly. Although the current results of the random roughness patch show similar near-field details as experiments,[7] the differences in size and persistence downstream of disturbances suggests that the simulated roughness may not allow the shear layer to develop the same as over the slightly rounded experimental roughness.

A less significant contribution to differences between DNS and experiments occurs due to the incoming Blasius flow in the DNS having a slight adverse pressure gradient (H=2.608) due to the closer proximity of the virtual flat plate to the suction wall than in previous simulations.[5,6] A value of H=2.591 indicates a perfect zero pressure gradient Blasius flow with values of H>2.591 corresponding to an adverse pressure gradient. In an adverse pressure gradient nearly-Blasius flow, the flow velocity at a given height is slower than it would be in a zero pressure gradient Blasius flow. This leads to

both an increase in the displacement thickness and a decrease in the momentum thickness, and thus an increase in the value for the shape factor. For a favorable pressure gradient, the flow velocity at a given height is faster that in a zero pressure gradient flow, leading to a decrease in the value for the shape factor.

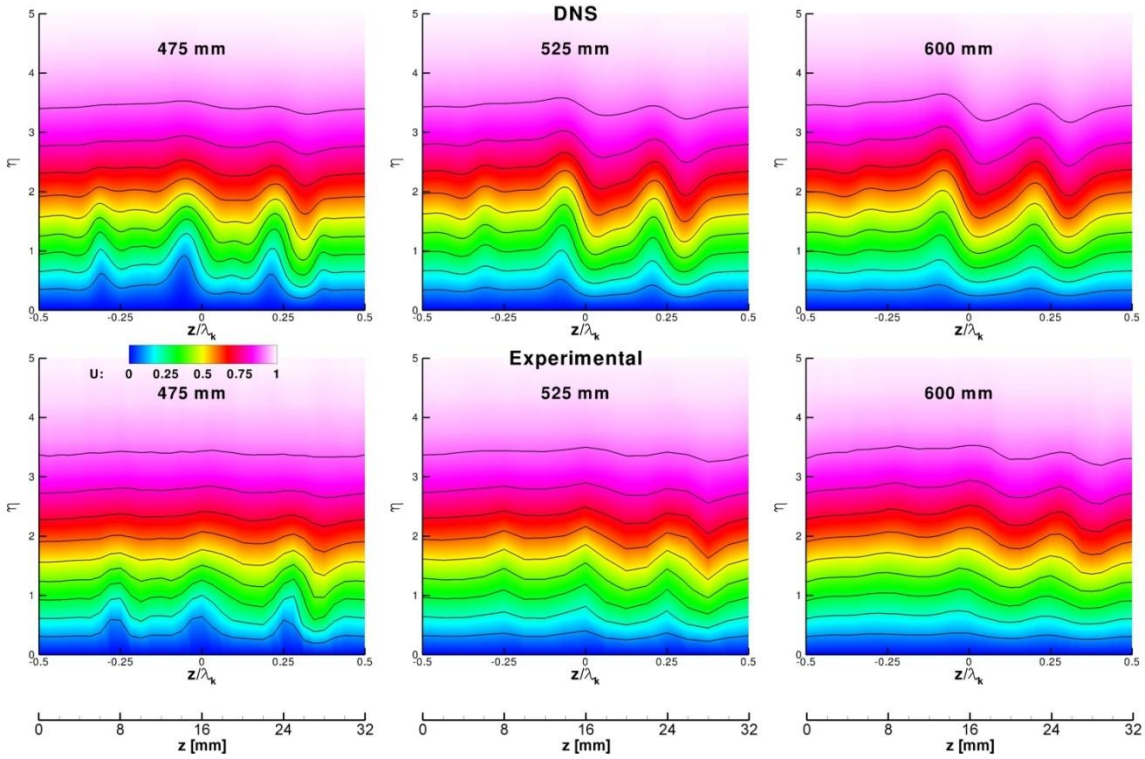

Figure 14: Re_k 164 streamwise velocity contours at x=475, 525, and 600 mm downstream of flat plate leading edge for both DNS and experiments. Contour lines in 10% U_∞ increments and colors are U.

The disturbances developed as the flow moves over the roughness patch are stronger than in the presence of a perfectly Blasius flow. Dassler et al. shows a similar correlation; in the presence of an adverse pressure gradient, the transition point due to sandpaper roughness moves upstream as a result of larger disturbances.[14] Not only does this create stronger disturbances, but dissipation of the disturbances is diminished as well.

The slightly favorable pressure gradient (H=2.58) in the incoming Blasius flow in experiments of Downs at al.[7] may help create smaller disturbances that dissipate quicker than those in the current DNS. This trend persists in the other values of Re_k simulated.

Both the DNS and experimental data in figure 14 show that disturbances which are near the wall in the 475 mm slice move upwards in the boundary layer as the flow continues downstream. This trend of the gradual upward displacement of the disturbance energy is also seen in the root mean square disturbance velocity profiles downstream of the roughness patch in figure 15. The disturbance velocity profiles (U'_{rms}) are calculated as

Here, $U(k)$ is the steady state local streamwise velocity at height k, $\bar{U}(k)$ is the local Blasius velocity at height k measured at the symmetry plane in the DNS and in between roughness patches in experiments, and n_z is the number of spanwise grid points. Disturbance velocities for the individual spanwise modes ($U'_{\lambda/m}$) are computed as the respective mode of the Fourier transform of U'_{rms}.

The rms disturbance velocity is useful for determining at what height above the flat plate the flow is most perturbed as well as relative strengths of these perturbations. The peak magnitude of the rms disturbance velocity not only decreases at further locations downstream, but it also moves up in the boundary layer. Figure 15 shows the possible effects of both the smoother experimental roughness and slightly differing incoming shape factors between DNS and experiments; peak magnitudes of U'_{rms} profiles in DNS are 25-35% larger than those in experiments.

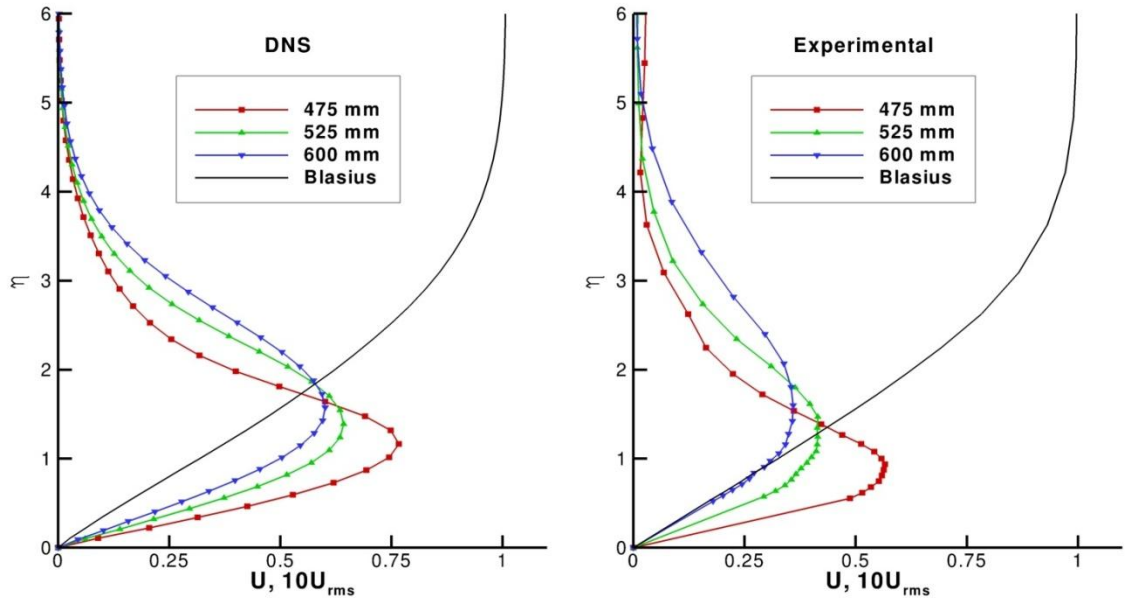

Figure 15: Root mean square disturbance velocity profiles for DNS and experiments at an Re_k of 164. Representative Blasius profile measured at the symmetry plane in DNS and in between roughness patches in experiments shown at 475 mm downstream of flat plate leading edge. Note: different x axis scales for rms disturbance velocities and Blasius velocities.

The disturbance energy profiles, calculated using equations 5 and 6 below, for the respective individual modes ($E_{\lambda/m}$) of the flow and root mean square (E_{rms}) undergo initial stable growth followed by decay further downstream of the roughness patch.

The E_λ profile, corresponding to the disturbance energy of the primary spanwise mode of the flow, has an initial spike created as the flow reaches the end of the roughness patch, immediately followed by rapid decay over about 10 mm (Figure 16). After the decay, downstream of ~x=500 mm, the profile stays at a constant value. The initial spike occurs because the λ wavelength accounts for disturbances spanning the entire spanwise domain. The $\lambda/2$ wavelength is largely unexcited for this geometry and value of Re_k; it remains near zero across the entire streamwise domain. Both the $\lambda/3$ and $\lambda/4$ wavelengths undergo growth over a 20-100 mm range beyond the roughness patch. The $\lambda/3$ wavelength reaches a plateau approximately 600 mm downstream of the flat plate leading edge while the $\lambda/4$ wavelength after its initial abrupt rise subsequently linearly decays towards zero. The three velocity deficit regions seen in figure 13 are approximately spaced $\lambda/3$ apart, causing the excitation of the $\lambda/3$ wavelength in the flow. Because these velocity deficit regions have little dissipation downstream, the excitation persists and $E_{\lambda/3}$ rises to a near-constant level. Since all the individual wavelengths do not undergo unstable growth, the root mean square disturbance energy profile does not undergo unstable growth either. The rms energy rises in an initial spike over the patch followed by rapid decay similar to the E_λ profile before leveling out at its final value. As in the experiments of Downs et al.[7], no transition to turbulence occurs and the flow remains laminar downstream of the roughness patch.

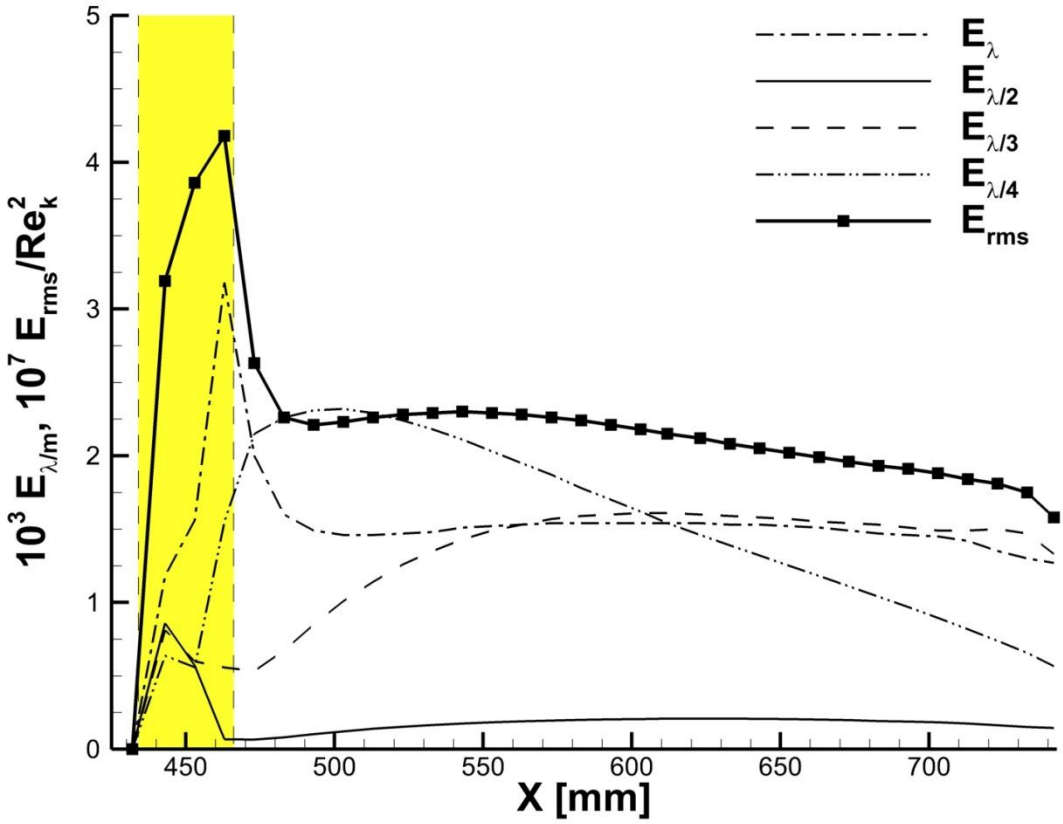

Figure 16: Disturbance energy profiles for Re_k 164 simulation. Yellow box represents location of roughness patch. Note: different y axis scales for individual wavelength and root mean square energies.

B. Re_k 227

The second simulation performed is at a U_∞ of 9.3 m/s, corresponding to an Re_k of 227. This value of Re_k falls just under the limit of stability (Re_k=250) found in previous experiments.[4,7] Larger lateral and vertical gradients are present in the flow than occurred for Re_k=164, however the flow remains laminar in both the DNS and experiments downstream of the roughness patch. Additional simulations for this value of Re_k are presented in later sections (chapter V, sections A and B) in an effort to better understand

the effect isolated regions of the overall roughness patch have on the near-field flow structures.

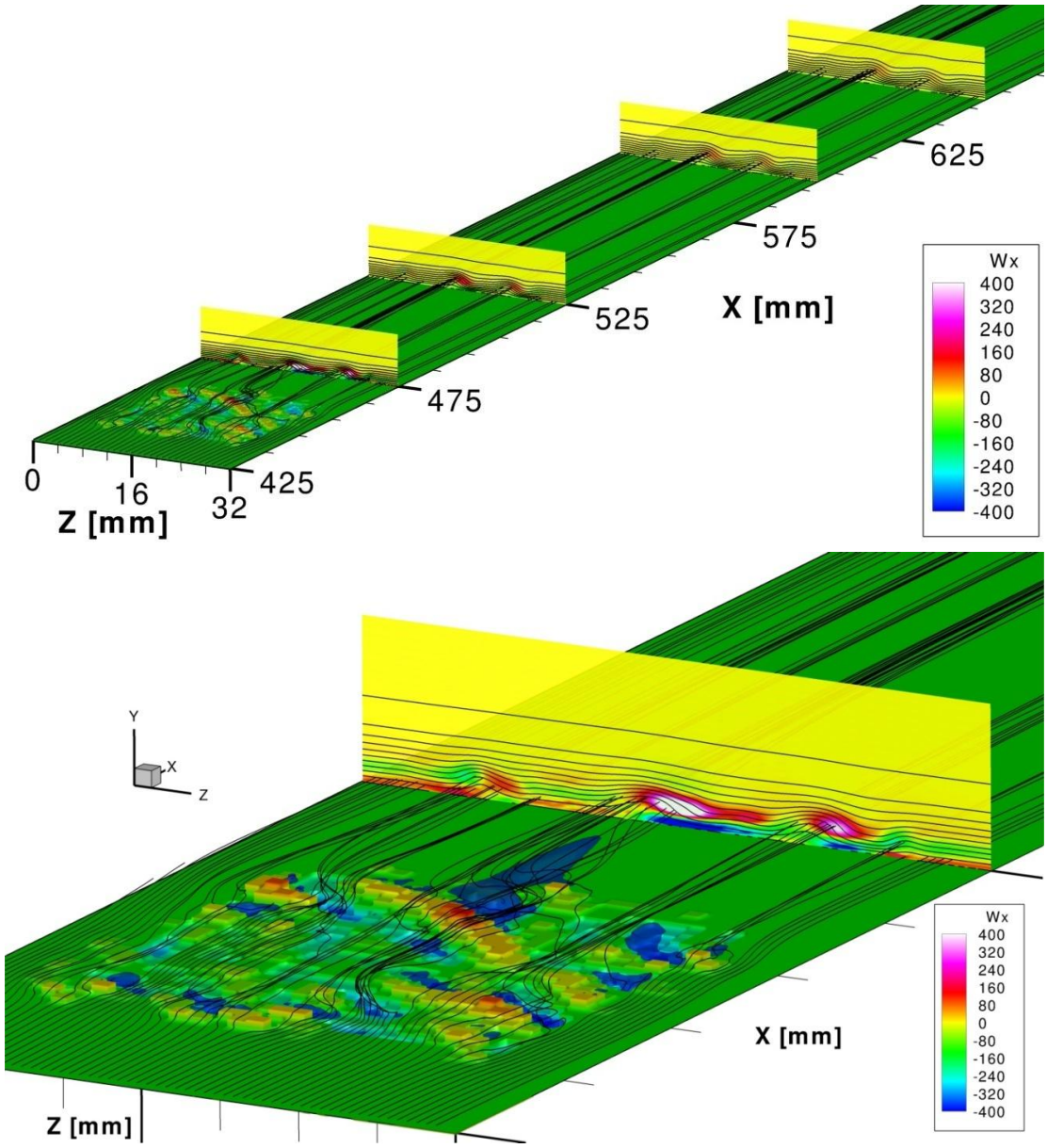

Figure 17: Top image shows overall flowfield for Re_k 227. Slices colored by ω_x with contour lines in 10% U_∞ increments. Roughness patch colored by height, streamlines at an initial height of y=0.25 mm shown in black. Bottom image shows detail of flow over the roughness patch and the x=475 mm slice. Blue iso-surface of negative U velocity shown. Other coloring is the same as in the top image.

Figure 17 shows the overall flowfield for the Re_k 227 simulation. Downstream slices are shown at x=475, 525, 600, and 650 mm from the flat plate leading edge. Comparison of the slices shows a relatively strong dissipation in downstream oriented vorticity as the flow moves downstream. Since the vortex cores pull slow moving flow from close to wall up into the boundary layer, this upwash effect is weakened as vorticity is dissipated. This can be more clearly seen when looking at the velocity contours presented in figure 18. The streamlines in figure 17 also show a clear tendency to orient themselves with the vortex cores created by the roughness patch. The streamlines coalesce around the vortex cores associated with the tallest regions of roughness. This is most readily seen when looking at the strongest vortex core near the B (z=14 mm) region of roughness in the detail of figure 17.

Velocity data are measured at 3 downstream locations (x=475, x=525, and x=600 mm downstream of the flat plate leading edge) in the simulation to compare against experiments. Figure 18 shows both DNS and experimental velocity data with contour lines in 10% U_∞ increments and colored by U. Of note is the increased magnitude of disturbances present in DNS. This may be due to the slight adverse pressure gradient present in the boundary layer as explained earlier in Chapter II. The data show good agreement at the 475 mm downstream location, however, at further downstream locations, the disturbances seen in experiments dissipate more than those in DNS. The data also show the disturbances moving up in the wall normal direction as the flow continues downstream. This appears to be due to the dissipation of downstream oriented vorticity near the wall. Moreover, the disturbances higher in the boundary layer (η~3) increase with increasing distance from the roughness patch.

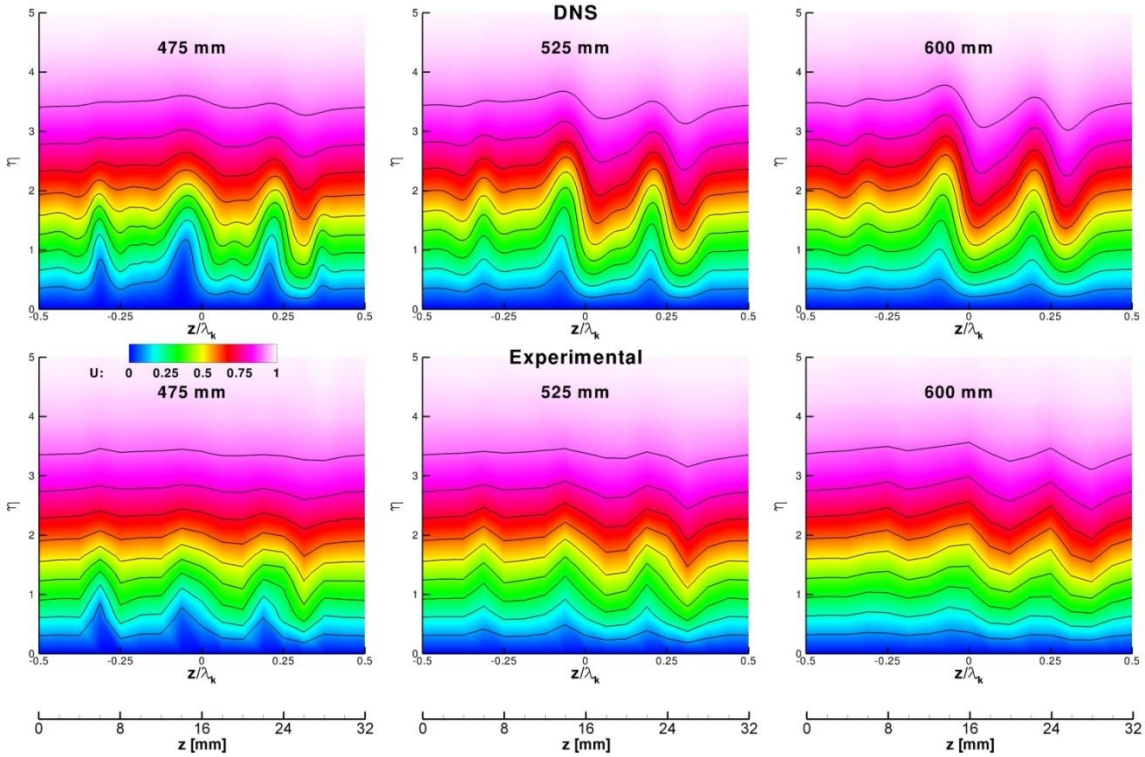

Figure 18: Re_k 227 streamwise velocity contours for both DNS and experiments. Images colored by U (blue=0 m/s, pink= U_∞) with contour lines in 10% U_∞ increments. Note: Image stretched vertically.

Detail of the 475 mm downstream slice structures is shown in figure 19. The three individual images focus on the near-field wake directly downstream of the three tallest regions of roughness present in the roughness patch. The images are stretched vertically by a factor of 1.4 with contour lines in 10% U_∞ increments and colors are by ω_x. Vectors are also shown to visualize locations and strengths of vortex cores.

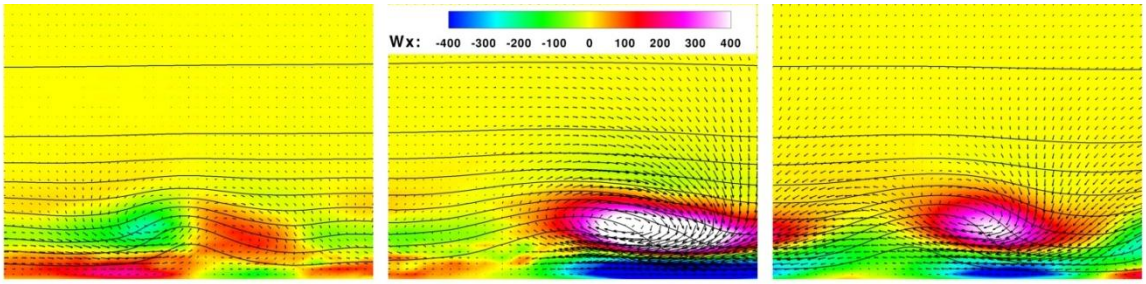

Figure 19: Detail of 475 mm downstream slice for Re_k 227. Contour lines in 10% U_∞ increments and colors are ω_x. Vectors shown to emphasize vortices. Left image corresponds to region of roughness centered at "A" (z/λ_k=-0.3), middle image centered at "B" (z/λ_k=-0.05), and right image centered at "C" (z/λ_k=0.2).

The tall region of roughness centered at z/λ_k=-0.05 ("B") produces the strongest vorticity, occurring as a single, asymmetric vortex core. The region of roughness centered at z/λ_k=0.2 ("C") also produces a single, asymmetric core at a lesser magnitude of downstream oriented vorticity. The tall region of roughness centered at z/λ_k=-0.3 ("A") produces a pair of weak symmetric vortex cores, similar to those seen in flow around a discrete cylindrical roughness element. The roughness upstream of the z/λ_k=-0.05 and z/λ_k=0.2 vortices is qualitatively similar to a swept ridge-like disturbance while the roughness upstream of the z/λ_k=-0.3 vortex pair has a more symmetric shape.

Figure 20 shows the rms disturbance velocity profiles at three x locations along with a representative Blasius profile measured as previously described at 475 mm downstream of a flat plate leading edge. The rms disturbance velocities have a higher peak value in DNS than experiments agreeing with the larger disturbances seen in figure 18. Despite the difference in magnitudes, both the experiments and the DNS data agree reasonably well when comparing overall trends. As the flow progresses downstream, the peak magnitudes of the disturbance velocities decrease and move further up in the boundary layer.

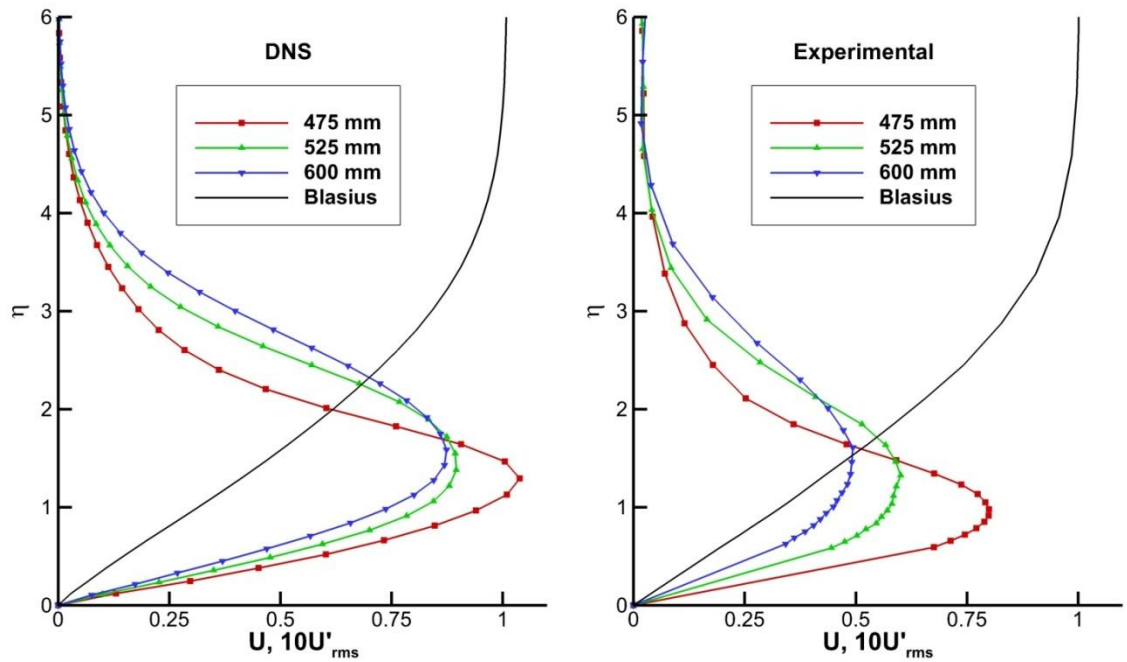

Figure 20: RMS disturbance velocities for Re_k 227. Note: different scales for U'_{rms} and $\bar{U}$ on the x axis.

Figure 20 shows more clearly that the peak amplitude of disturbances occurs close to the wall just downstream of the roughness patch but it gradually moves up in the boundary layer at further downstream locations. We next examine the disturbance energies for each of the first four characteristic spanwise modes and the overall rms disturbance energy.

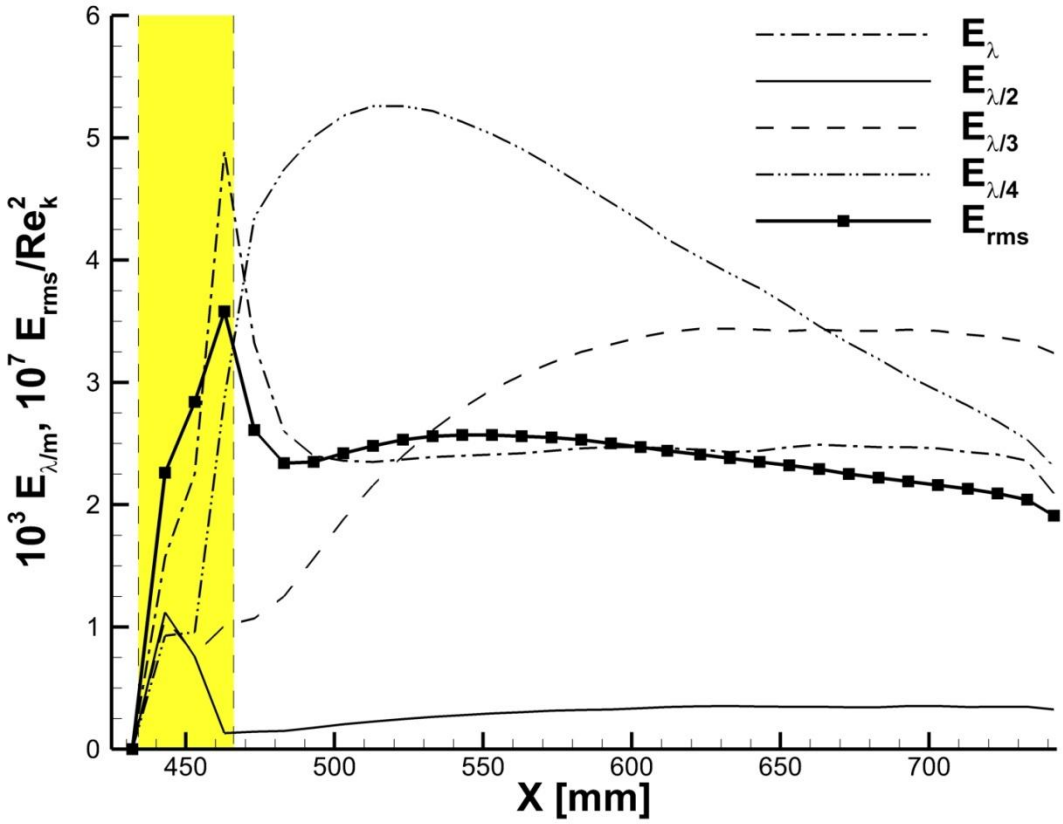

Figure 21: Disturbance energies for Re_k 227. X axis measures downstream location from flat plate leading edge (in mm). Roughness patch location shown as yellow box. Note: different scales for y axis.

Figure 21 indicates a strong initial increase in the $\lambda/3$ and $\lambda/4$ modes and a rapid rise followed by decay in the λ wavelength. It is not surprising that the $\lambda/4$ mode undergoes the most excitation because the tallest regions of roughness (z/λ_k=-0.3, -0.05, and 0.2, respectively) are approximately separated by $\lambda/4$ mm. This rise in $\lambda/4$ energy is followed by a steady decrease as downstream oriented vorticity dissipates and the far-field wake takes on its final steady state shape. It is interesting to note that the $\lambda/2$ mode has very little energy associated with it.

Comparing E_λ and E_{rms}, one can see a strong initial spike at the trailing edge of the roughness patch, followed by a rapid decay to steady state values. Because both the λ wavelength and total rms depend on the entire spanwise domain, they both exhibit very similar trends. The initial spikes occur due to the rapid changes in the flow from an incoming Blasius profile to the highly perturbed flow over the roughness patch. As the flow reorganizes itself and near-field flow structures are fully developed, the flow once again reaches a quasi-steady state and thus the energies on the scale of the entire spanwise domain quickly dissipate to their final values. There is no transition to turbulence for Re_k 227. This is expected, however, as the value for the height-based Reynolds number falls below the limit for stability of 250.

C. Re_k 301

Finally, a simulation is performed at an Re_k of 301. This value was chosen because it is above the threshold for potential transition to turbulence downstream of the roughness patch. In the experiments performed by Downs et al., transition occurred approximately 525 mm downstream of the flat plate leading edge. The overall flowfield of the simulation is presented in figure 22.

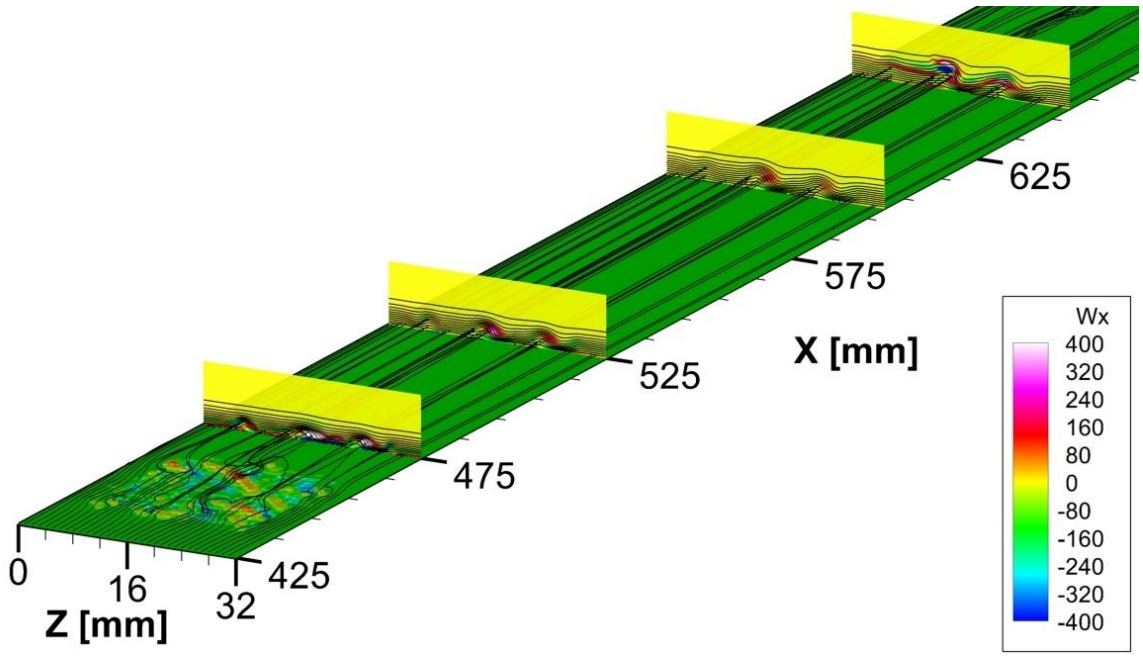

Figure 22: Overall instantaneous flowfield for Re_k 301. Slices are colored by ω_x with contour lines in 10% U_∞ increments. Note: slices and streamlines are time averaged because of turbulence.

Figure 22 shows stronger downstream oriented vorticity than in lower Re_k simulations with less dissipation occurring downstream. The slice at 650 mm shows large gradients in ω_x and a clear unsteady nature to the instantaneous streamlines beyond this point. Detail of the flow over the roughness patch and the 475 mm downstream slice is shown in figure 23. The blue iso-surface behind the middle region of tallest roughness, representing negative streamwise velocities, is much larger than in the two lower Reynolds number simulations. Thus, a larger recirculation region is present along with stronger vorticity.

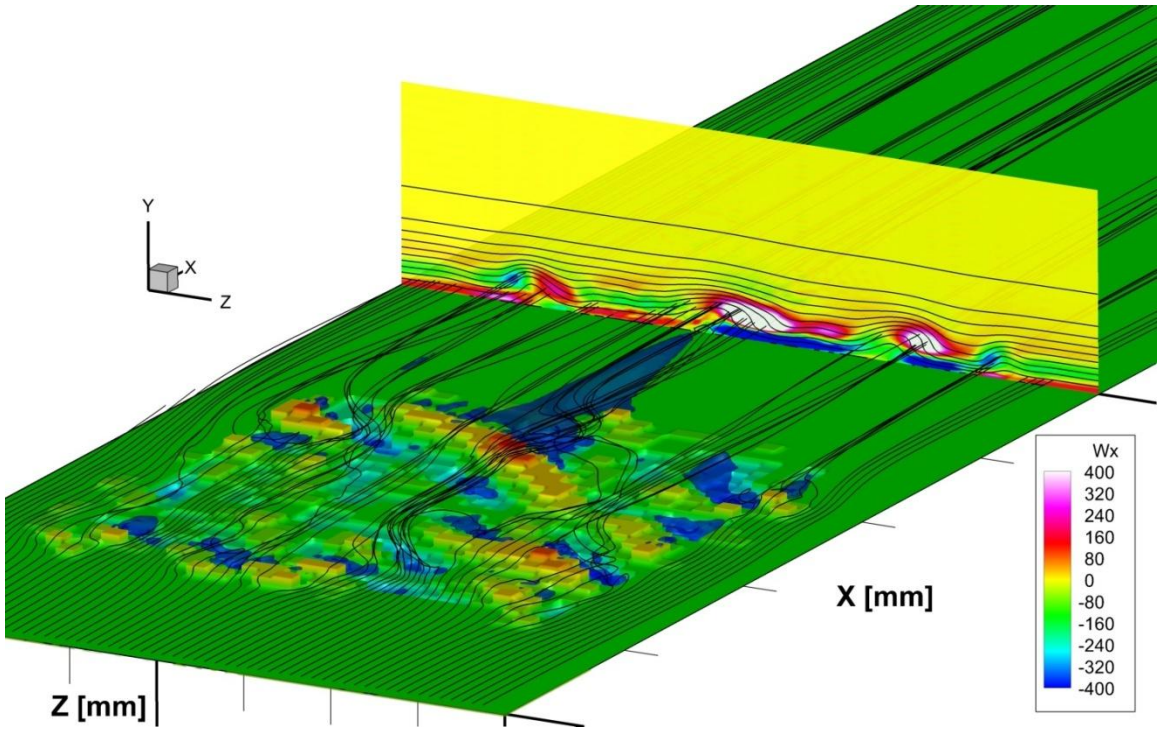

Figure 23: Detail of flow over roughness patch for an Re_k of 301. Negative streamwise velocities shown as blue iso-surface. Other coloring and contour lines are same as in figure 21.

To determine where transition occurs in the simulation, λ_2 is calculated for several instantaneous time steps. λ_2 is a useful definition of swirl strength to highlight vortices in incompressible flow. It is calculated as the second eigenvalue of the sum of the squares of the symmetric and antisymmetric parts of the velocity gradient tensor $\boldsymbol{u}$. More information on λ_2 can be found in Jeong and Hussain.[22] Figure 24 shows downstream detail of λ_2 at 75,000 time steps (5.5 flow-throughs). Both elongated tubes and fully developed horseshoes are seen in the λ_2 iso-surfaces. The initial transition to turbulence occurs among the elongated tubes of vorticity in the range of 625 to 700 mm downstream of the flat plate leading edge. These elongated tubes then start spreading laterally into a wedge shape around 700 mm downstream of the flat plate leading edge, indicating the

breakdown of the flow to a turbulent state. It is in this turbulent wedge that λ_2 hairpins or arches form, with similar structures to other studies in turbulence.

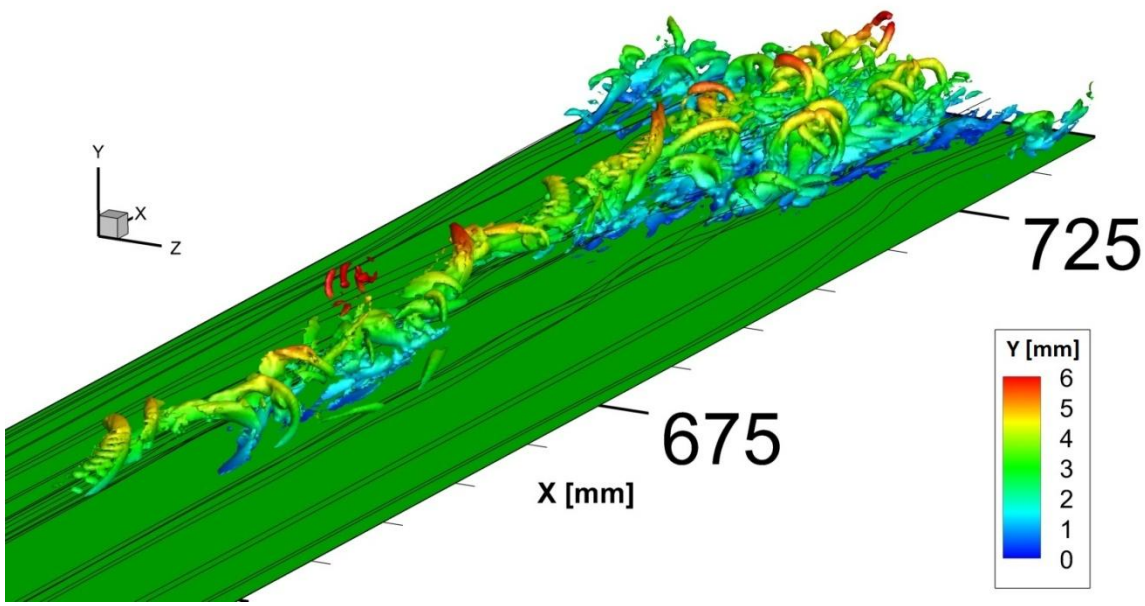

Figure 24: Downstream detail, 610-743 mm, of Re_k 301 simulation. Iso-surface of λ_2=-0.3 shown with coloring by y indicated by legend.

Due to the single component hotwire used in experiments, only streamwise (U) velocity contours can be directly compared between DNS and experiments (Figure 25). The DNS slices are time averaged over the last 8,000 time steps to remove some temporal variations because the data collected by the hotwire was time averaged over a long period. The 475 mm downstream slices agree well, showing three distinct velocity deficit regions caused by the vortical structures formed as the flow moves over the roughness patch. As the flow continues downstream, the magnitude of the velocity deficit regions for the DNS does not dissipate as fast as in experiments. Once again, this is most likely due to the sharp cusps present in the DNS roughness creating stronger

disturbances. At 525 mm downstream, the disturbances higher in the boundary layer, η of between 2 and 3, agree fairly well with experiments. However, the near wall disturbances have been more strongly dissipated in the experiments.

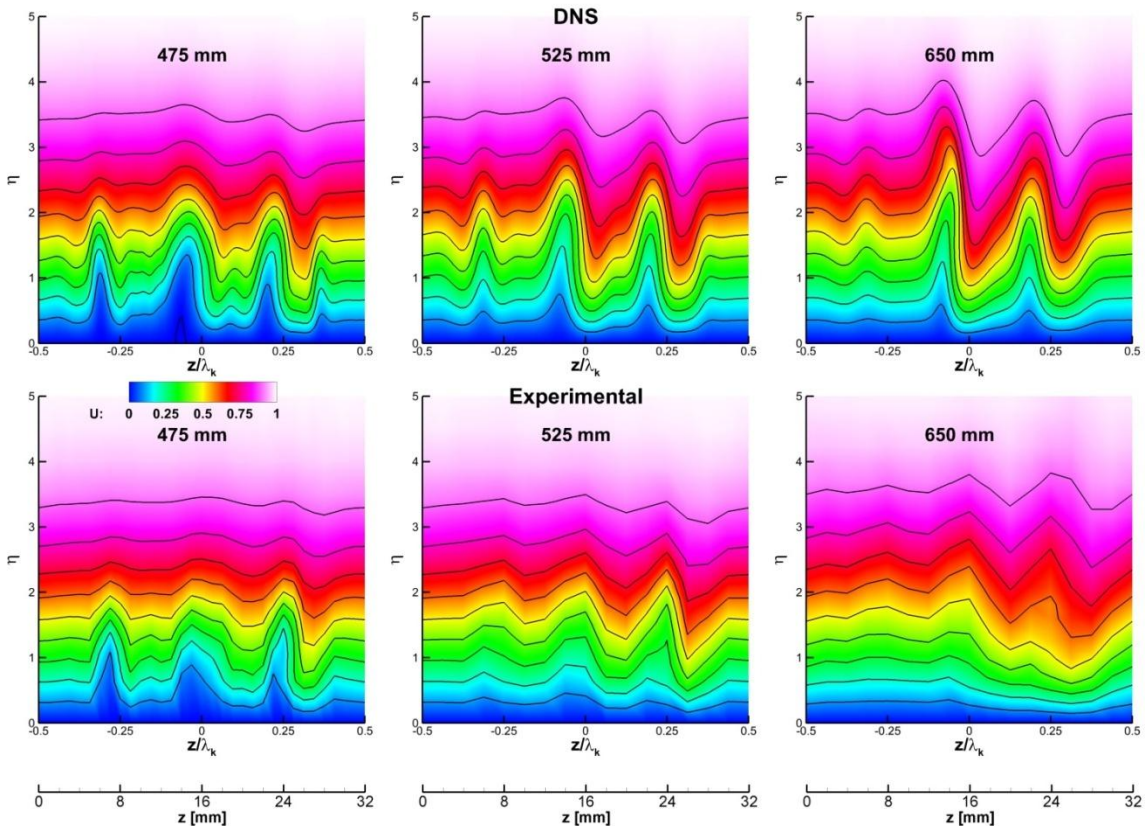

Figure 25: Streamwise velocity contours for an Re_k of 301. Contour lines are in 10% U_∞ increments and colors are U. Note: third slice taken at 650 mm instead of 600 mm to ensure data was taken downstream of transition point.

The third slice is taken at 650 mm for Re_k 301 as opposed to 600 mm in lower Re_k simulations. This is done to ensure that data are taken downstream of the transition location. At 650 mm, DNS and experimental data show surprisingly different results. DNS data continue to show two large velocity deficit regions at z/λ_k=-0.05 and z/λ_k=0.2, respectively, with a third weak disturbance at z/λ_k=-0.3. This same result is seen in the

lower Re_k simulations as well. Experimental data, however, show accelerated flow near the wall between z/λ_k=0 and z/λ_k=0.5 with slight velocity deficit regions higher up in the boundary layer at z/λ_k=-0.05 and z/λ_k=0.2. These discrepancies can likely be attributed to the large temporal fluctuations present in both DNS and experiments. Figure 26 shows the 650 mm downstream slice for both DNS and experiments. Experimental data show larger u'_{rms} magnitudes over a larger portion of the slice than does the DNS. Figure 26 also shows temporal variation occurring near the centerline in the DNS. This is due to the location of the slice relative to the transition point. A DNS slice taken further downstream will show more pronounced temporal variations across the entire spanwise extent as the turbulent wedge continues to spread in the spanwise direction as the flow continues downstream.

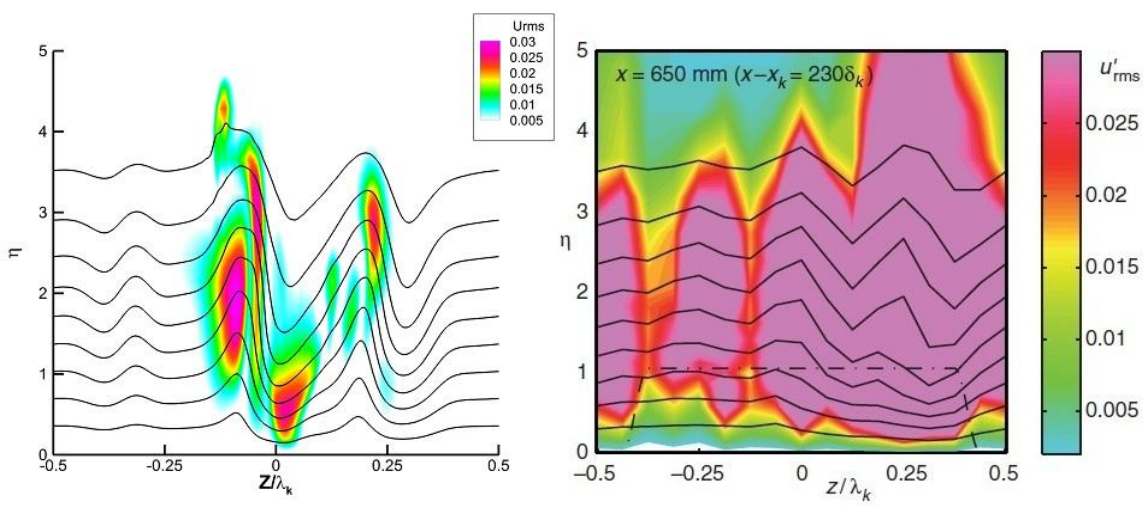

Figure 26: Re_k 301 650 mm downstream slice for DNS and experiments. Contour lines in 10% U_∞ increments and colors are u'_{rms}.

It should be expected that the span-averaged U'_{rms} profiles for DNS will have larger magnitudes than for experiments based on the velocity contours in figure 25. This

proves to be true and is seen in figure 27. For all three downstream locations, the DNS U'_{rms} profile reaches an approximately 25% larger peak magnitude than in experiments.

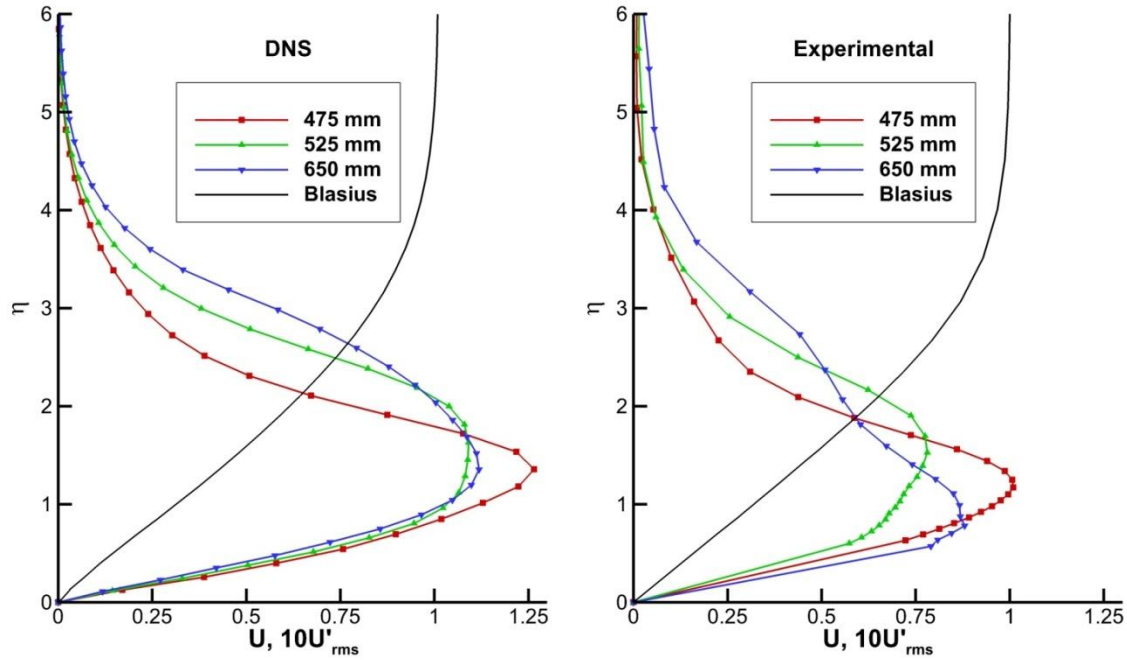

Figure 27: Root mean square disturbance velocities for Re_k 301. Note: different x axis scales for $\bar{U}$ and U'_{rms}.

Transition to turbulence occurs between 625 and 700 mm downstream of the flat plate leading edge in simulations as previously visualized in figure 24. The transition occurs when an unsteady growth of the λ and $\lambda/2$ wavelengths occurs. Figure 28 shows that these wavelengths' disturbance energy contributions remain flat and stable until transition occurs. Once the flow reaches the transition region, the λ and $\lambda/2$ wavelengths energy components rise tremendously. The shorter flow wavelengths, $\lambda/3$ and $\lambda/4$ do not undergo the same type of excitation. Upstream of the transition region, the $\lambda/3$ and $\lambda/4$ wavelengths have similar profiles to the previous Re_k 227 simulation. After transition, the profiles show an overall decay in energy with some smaller scale oscillations.

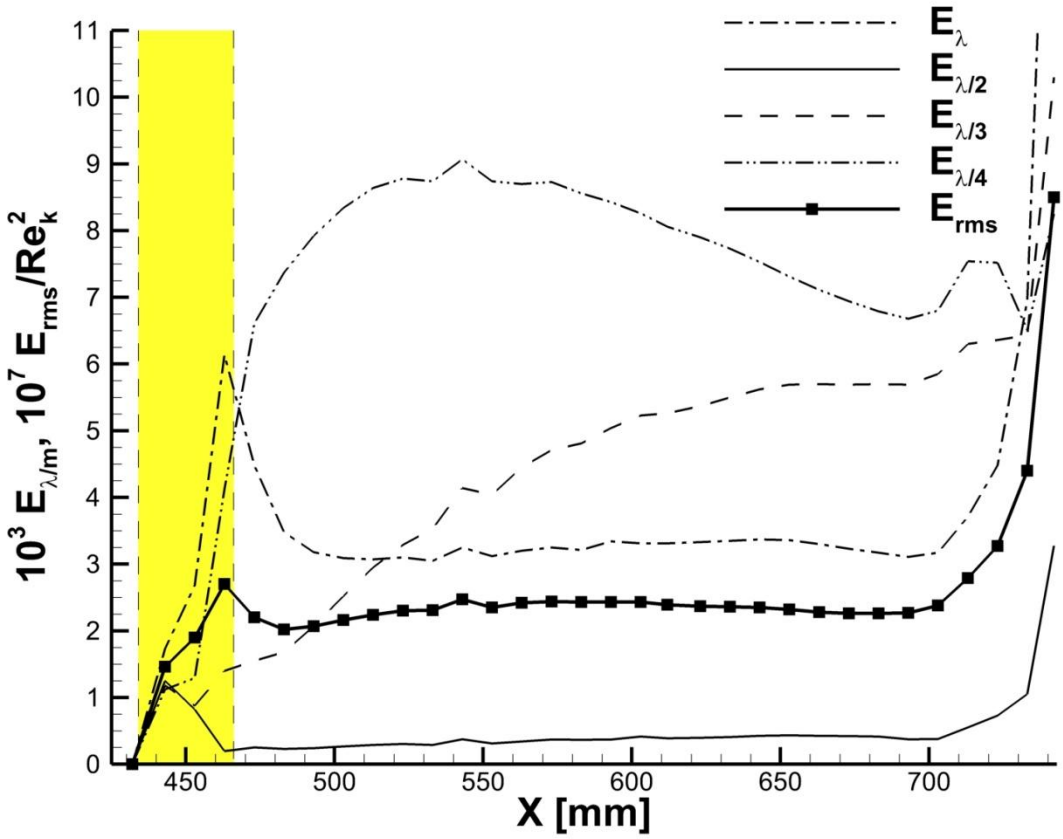

Figure 28: Disturbance energy profiles for Re_k 301 simulation. Profiles are time averaged over 8000 time steps and show a mean transition location of approximately 650 mm downstream of flat plate leading edge. Note: different y axis scales for individual wavelengths and rms energies.

The results presented in the current Re_k 301 section are time averaged over only 8000 time steps (0.59 flow-throughs). Near the transition region, the flow is only marginally turbulent; the flow will transition to turbulence, relaminarize, transition again, and continue in this manner. Due to the chaotic nature of turbulent flow, much more flow time needs to be included in the averaging to make a better comparison to the experiments.

V. SMALL SCALE ROUGHNESS INVESTIGATION

What exactly is roughness made of? How do the smaller regions of the roughness interact to create the near-field details? Would removal of certain elements of the roughness drastically change the results? An investigation of the smaller scale geometric features of the roughness patch simulated can lead to a better understanding of how flow features interact in the near-field, and thus a better understanding of their contribution to transient growth.

A. Re_k 227 Alternate Geometries

Two distinct geometries are simulated for an Re_k of 227 to compare against the full roughness patch run in the previously presented simulation results and experiments. The first alternate roughness patch (slip surface) is shown in the top left image of figure 29. This roughness patch replaces all of the non-positive amplitudes ("valleys") with a surface allowing streamwise and spanwise slip (shown in gray), however a no through flow condition still exists in the wall normal direction. This is done to examine the effects of the valleys on the near-field structures and wake downstream of the roughness patch. The second alternate roughness patch ("tall roughness only") is shown in the top right image of figure 29. This roughness patch leaves only the three regions of tallest roughness, replacing everything else with a non slip, no through flow surface at the flat plate height. This is done to determine if these tallest regions are the driving factor of the near-field details and what effect the smaller roughness has, if any.

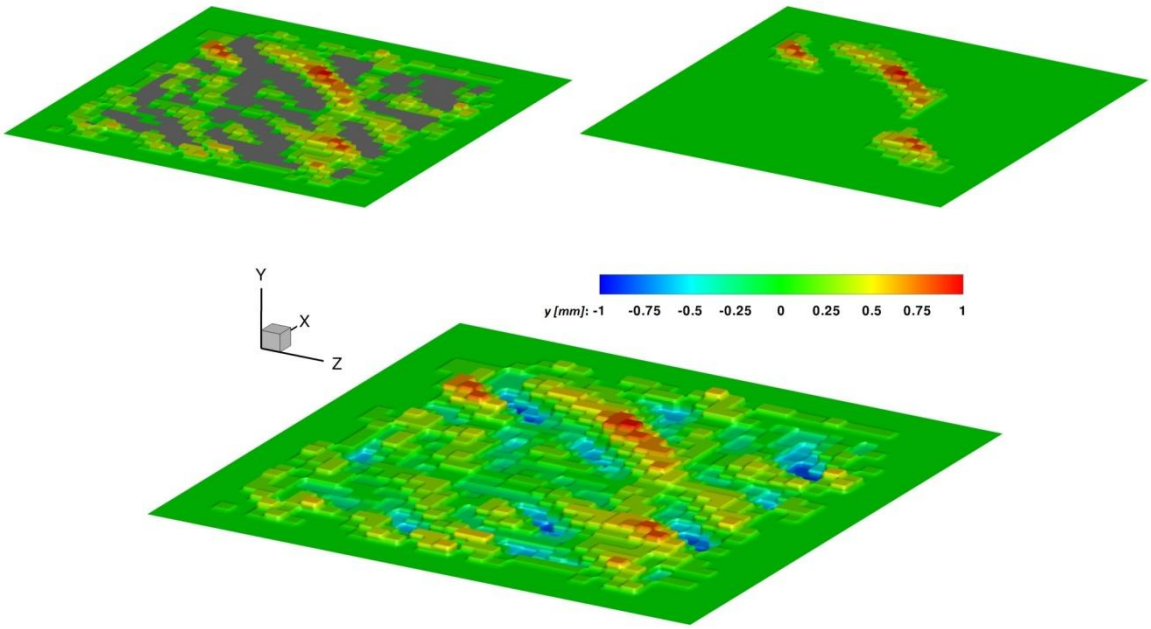

Figure 29: Comparison of alternate geometries simulated. Top left image shows slip surface geometry where non-positive amplitude perturbations are replaced by a spanwise and streamwise slip surface shown in gray. Top right image shows "tall roughness only" ("TRO") geometry where only the 3 regions of tallest roughness remain. Bottom image shows original roughness patch geometry for comparison purposes. Note: bottom image sized 150% of top images to show detail.

First, the Re_k 227 simulation with the full roughness patch is compared against the Re_k 227 simulation with the slip surface roughness patch. This is performed to determine the effect of the valleys on the roughness geometry. When flow moves in the valleys, a non-zero velocity can exist at the flat plate height, causing a shear layer to develop when the flow reaches a section of the roughness which is at the flat plate height. The slip surface geometry allows for similar circumstances to occur, although no wall normal velocity is allowed on the slip surface itself. Figure 30 shows the in-plane, $(U^2+W^2)^{1/2}$, flow velocity at the flat plate height for slip surface geometry on top and full roughness geometry on bottom. The in-plane velocity magnitude is nearly identical to that for both

geometries. This indicates that the slip surface functions in the same manner as the "valleys" in the fully modeled roughness geometry; flow at the mean plate height over the "valleys" has non-zero velocity.

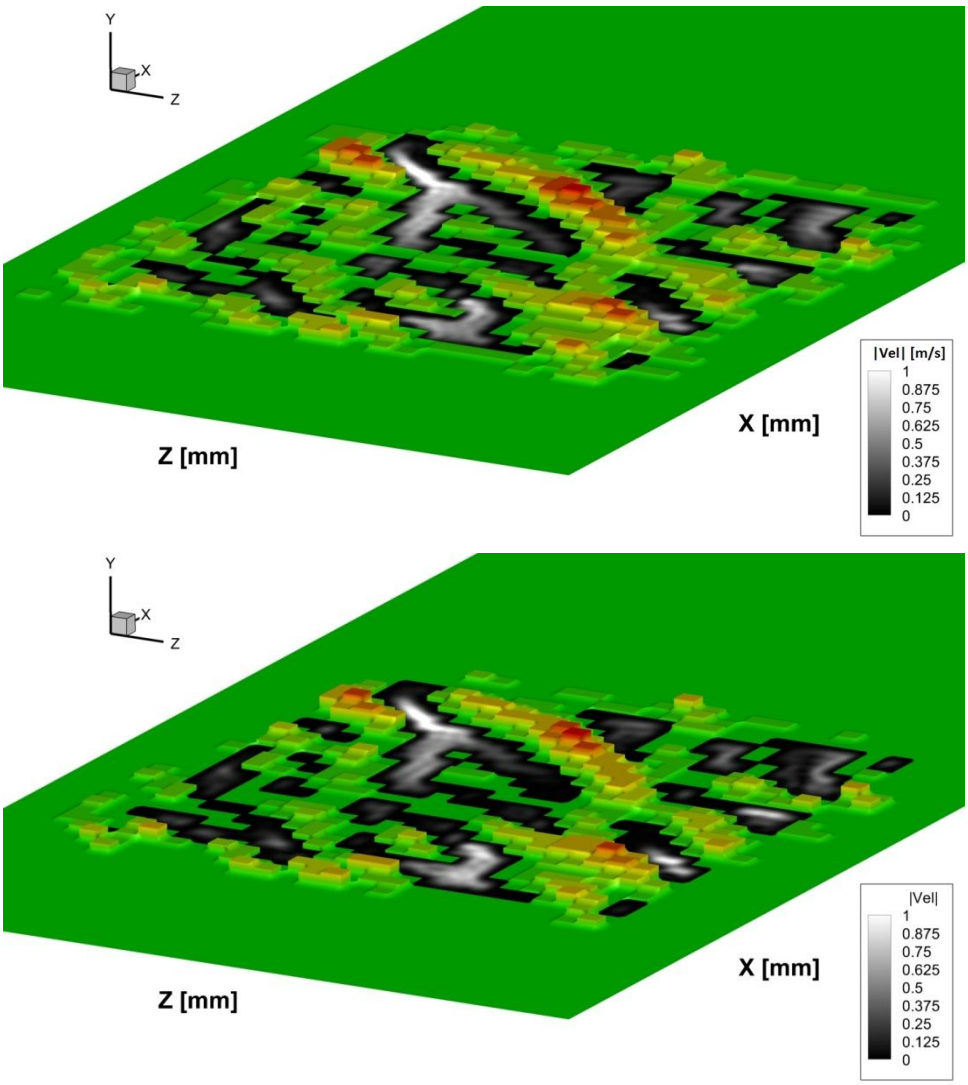

Figure 30: Top image shows in-plane velocity magnitude at mean flat plate height over slip surface geometry. Bottom image shows in-plane velocity magnitude at mean flat plate over the "valleys" in the full roughness geometry. Roughness coloring is the same as in figure 28.

From figure 30, it is clear that the slip surface allows for the flow in the roughness patch itself to develop in much the same way as the full roughness geometry. One difference occurring between the two geometries is the vorticity at the mean plate height. Although the slip surface allows both spanwise and streamwise velocities to exist at the flat plate height, it still enforces a no through flow condition in the wall normal direction. This does not allow for the vorticity to develop in an identical manner as it does in the fully modeled roughness geometry because flow cannot dip into the valleys where a slip surface is present.

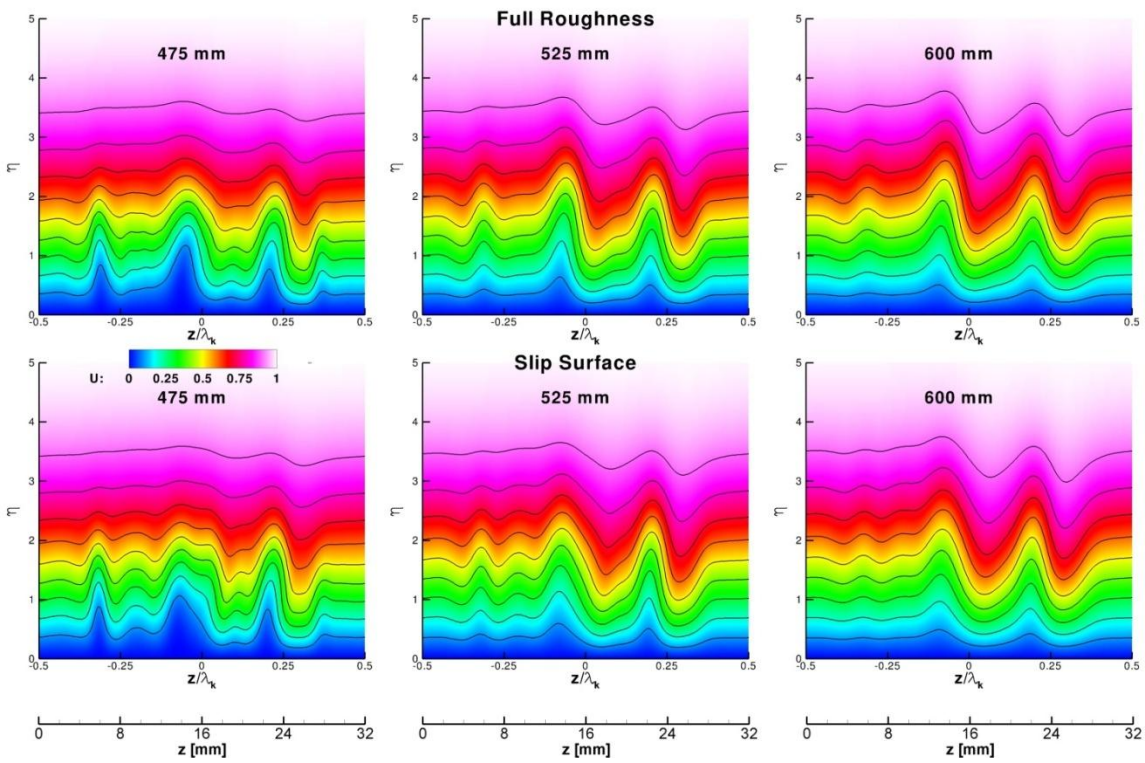

Figure 31: Streamwise velocity contours for the fully modeled roughness (top) and slip surface (bottom) geometries at an Re_k of 227. Contour lines are in 10% U_∞ increments and colors are U.

Streamwise velocity contours are presented in figure 31 for both the full roughness and slip surface geometries at 475, 525, and 600 mm downstream of the flat plate leading edge. The velocity disturbances are very similar in both magnitude and shape. Both geometries give rise to three strong velocity deficit regions with minor differences in shape due to the variation in the vorticity formed as the flow passes over the roughness.

Figure 31 shows a small velocity deficit at z/λ_k=-0.22 in the slip surface geometry that is not present in the full roughness results. To better understand the origin of this velocity deficit, downstream oriented vorticity is shown in figure 32. The full roughness geometry produces a single asymmetric core as the flow turns past the region of tall roughness at z/λ_k=-0.05, whereas as a weak counter rotating vortex occurs alongside the strong asymmetric core at this spanwise location in the slip surface geometry. This may be due in part to the boundary conditions of the slip surface geometry not allowing a vertical velocity to exist at the flat plate height as well as a difference in vorticity upstream of the tall roughness. Despite this minor difference between the two geometries, the flow in the valleys of the full roughness patch is well modeled as a surface at the flat plate height allowing spanwise and streamwise slip.

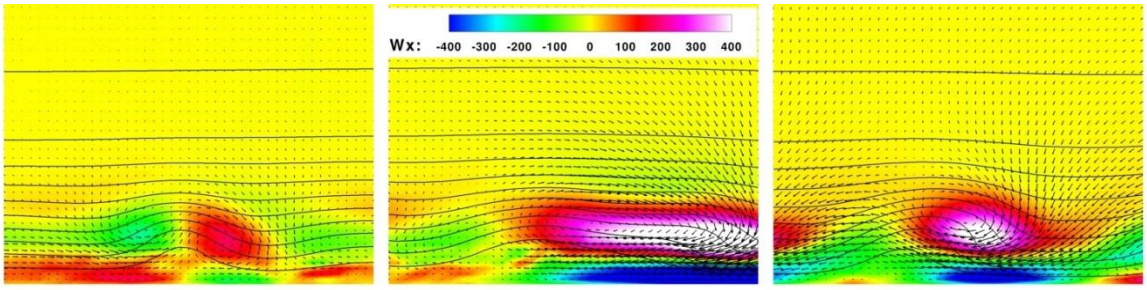

Figure 32: 475 mm downstream slice for the slip surface geometry at an Re_k of 227. Contour lines are in 10% U_∞ increments and colors are ω_x.

In order to verify that the two flows are indeed similar, further investigation into the disturbance velocities and energies is performed. The rms disturbance velocities are calculated as they were previously and shown in figure 33. The profiles are almost identical at all locations downstream. Peak magnitudes and heights of the disturbance velocity profiles agree well, indicating the negative amplitudes of the full roughness geometry and the spanwise and streamwise slip surface have negligible effects on the flow. This is an important result in understanding what contribution the individual portions of the full roughness geometry have on the near-field details of flow past realistic roughness.

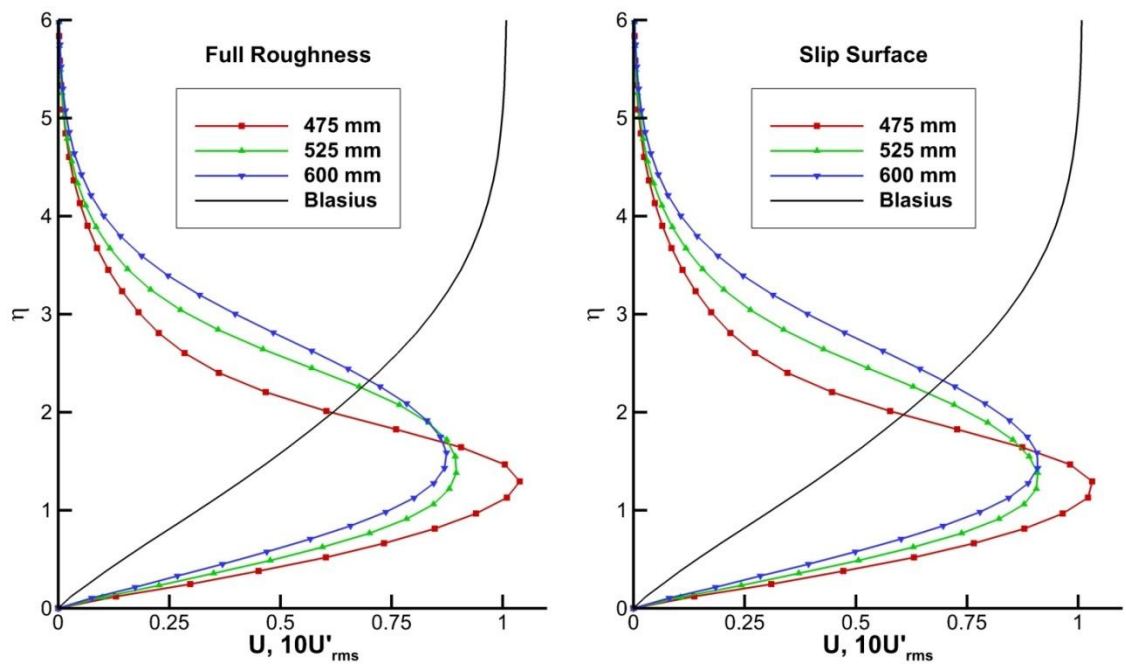

Figure 33: RMS disturbance velocity profiles for both the fully modeled roughness and slip surface geometries. Note: different x axis scales for $\bar{U}$ and U'_{rms}.

Comparing figure 34 to figure 21 in the Re_k 227 full roughness geometry reveals almost identical results. The $\lambda/2$ wavelength is unexcited throughout the entire domain while the λ wavelength undergoes an initial spike and rapid decay before quickly settling

to its final value within 50 mm downstream of the roughness patch. The *λ/4* wavelength is excited by the flow before linearly decaying over the last two-thirds of the domain. The *λ/3* wavelength is excited over the first half of the domain before reaching a plateau over the second half. The rms disturbance energy shows an initial spike and exponential decay similar to the *λ* wavelength before remaining essentially constant. As in the full roughness geometry at an Re_k of 227, the slip surface geometry also does not transition to turbulence at any point in the domain.

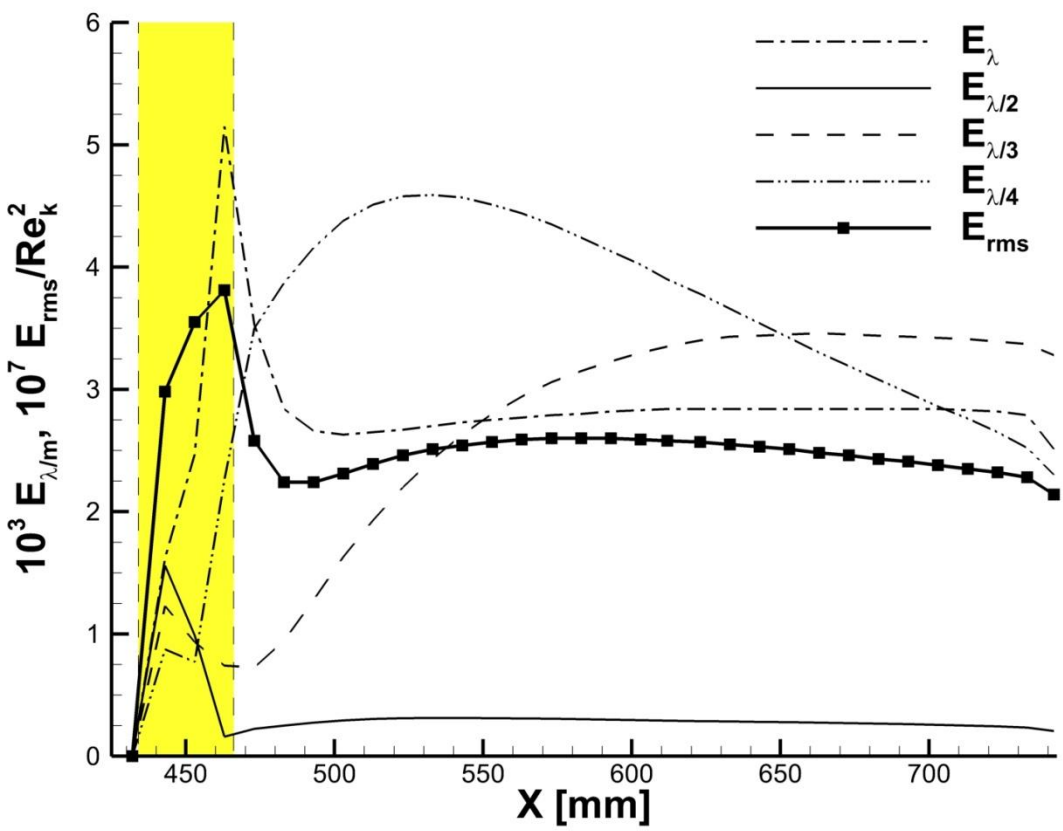

Figure 34: Disturbance energies for both individual flow wavelengths and rms for the slip surface geometry. Note: different y axis scales for E_λ and E_{rms}.

The second comparison performed is between the Re_k 227 full roughness geometry and the "tall roughness only" ("TRO") roughness geometry. The purpose of

this comparison is to determine what effect, if any, the shorter positive roughness heights have on the near-field details. The overall flowfield for the "tall roughness only" geometry is shown in figure 35. Comparing these results to those of both the Re_k 227 full roughness and slip geometries, it is evident that the "tall roughness only" flow experiences much larger perturbations. Also, downstream oriented vorticity dissipates at a slower rate than in the other simulations.

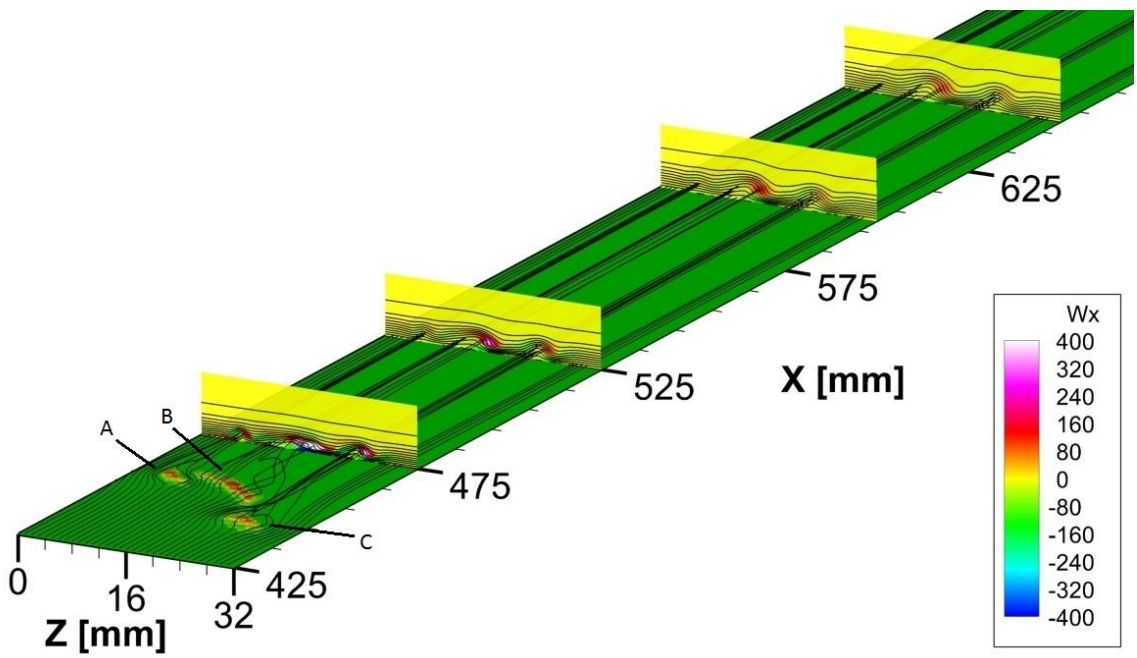

Figure 35: Overall flowfield for "tall roughness only" geometry. Slices are colored by ω_x with contour lines in 10% U_∞ increments.

Streamwise velocity contours are compared against the Re_k 227 fully modeled roughness geometry and presented in figure 36. The velocity contours once again show the three distinct velocity deficit regions associated with the three tallest regions of roughness occurring at approximately the same spanwise locations; however, the disturbance at z/λ_k=-0.05 is considerably larger in the "tall roughness only" geometry.

This appears to be due to the lack of shorter roughness upstream of the tall region B, as well as a lack of "valleys." The flow just upstream of the tall region, B, of roughness at z/λ_k=-0.05 is still Blasius in this "TRO" geometry as opposed to slightly perturbed in the full roughness and slip surface geometries.

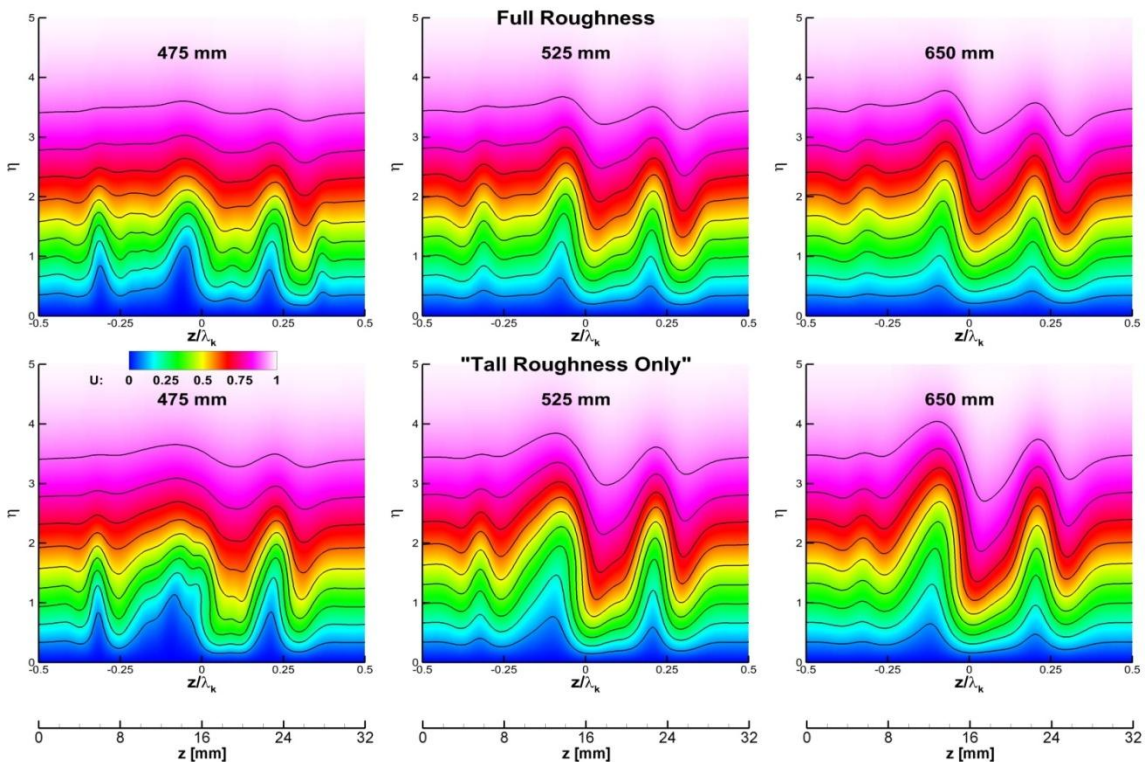

Figure 36: Streamwise velocity contours comparing the R_{ek} 227 full roughness geometry to the "tall roughness only" roughness geometry. Velocity contour lines are in 10% U_∞ increments and colors are U.

Figure 37 shows a detail of data at 475 mm downstream of the flat plate leading edge for the "tall roughness only" geometry with contour lines in 10% U_∞ increments and colored by ω_x. The three velocity deficit regions are created by the same pattern of vortices seen in the full roughness and slip surface geometries. However, because the incoming flow does not have any smaller roughness upstream or downstream of the tall

regions A, B, and C present in the "tall roughness only" geometry, the vorticity created is stronger than in previous geometries. This creates larger disturbances as the slower moving flow near the wall can thus be lifted higher in the wall normal direction than can be done by weaker vortices.

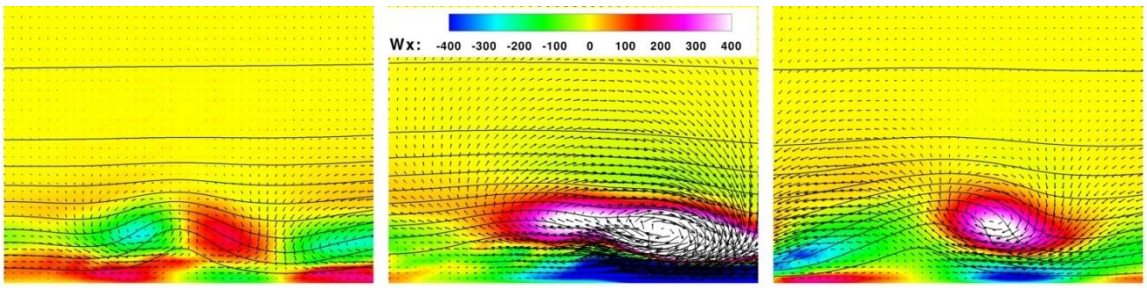

Figure 37: 475 mm downstream detail for "tall roughness only" geometry. Contour lines are in 10% U_∞ increments and colors are ω_x.

Since the velocity deficit regions are larger in the "tall roughness only" geometry than the full roughness geometry at an Re_k of 227, it is not surprising that the disturbance velocity profiles shown in figure 38 reveal a similar trend. The rms disturbance at 475 mm is approximately 25% larger for the "tall roughness only" geometry and the rms disturbances at 525 and 600 mm are approximately 35% larger. Also, there is no substantial dissipation in the peak rms disturbance as the flow moves downstream. This is contrary to what is seen in the other geometries and occurs because of the lack of dissipation of downstream oriented vorticity. Although the local vorticity peak near the wall rises higher in the boundary layer as the flow moves downstream, its magnitude remains largely unchanged. This is possibly due to the initial disturbances approaching the instability point where transition to turbulence may occur. If the freestream velocity is increased by a small amount, the flow may transition in the "tall roughness only" geometry.

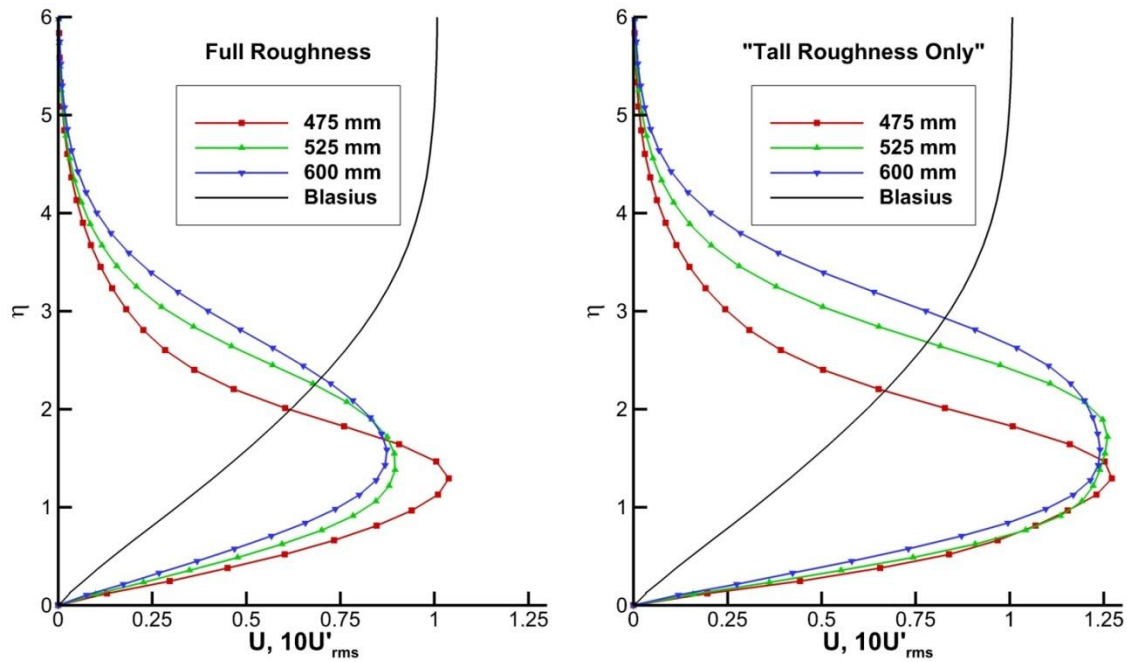

Figure 38: RMS disturbance velocity profiles for Re_k 227 full roughness and "tall roughness only" geometries. Note: different x axis scales for $\bar{U}$ and U'_{rms}.

The disturbance energies are calculated for the λ-$\lambda/4$ wavelengths and root mean square and shown in figure 39. These energies associated with the "tall roughness only" geometry are at much higher levels than those for the full roughness geometry. As in the previous geometries, the $\lambda/3$ wavelength undergoes the largest energy growth before steadying at around 600 mm downstream of the flat plate leading edge. The main difference in the $\lambda/3$ wavelength between the "tall roughness only" and full roughness geometry is its peak value. For an Re_k of 227, the peak value of the energy associated with the $\lambda/3$ wavelength is around 3, but in the "tall roughness only" geometry, it is around 12. The $\lambda/2$ wavelength also shows a different trend in this geometry than in the full roughness geometry. Previously, the $\lambda/2$ wavelength was largely unexcited, showing no growth over the entire domain. In the "tall roughness only" geometry, the $\lambda/2$ wavelength undergoes a steady growth through 650 mm downstream of the flat plate

leading edge. The increase in the *λ/2* and *λ/3* energies occurs as a result of the unperturbed flow both upstream and downstream of the three isolated roughness regions in the "tall roughness only" geometry. Although the largest increases in peak energy between the "tall roughness only" and full roughness geometries occur for the *λ/2* and *λ/3* wavelengths, all other wavelengths and the rms undergo an increase as well.

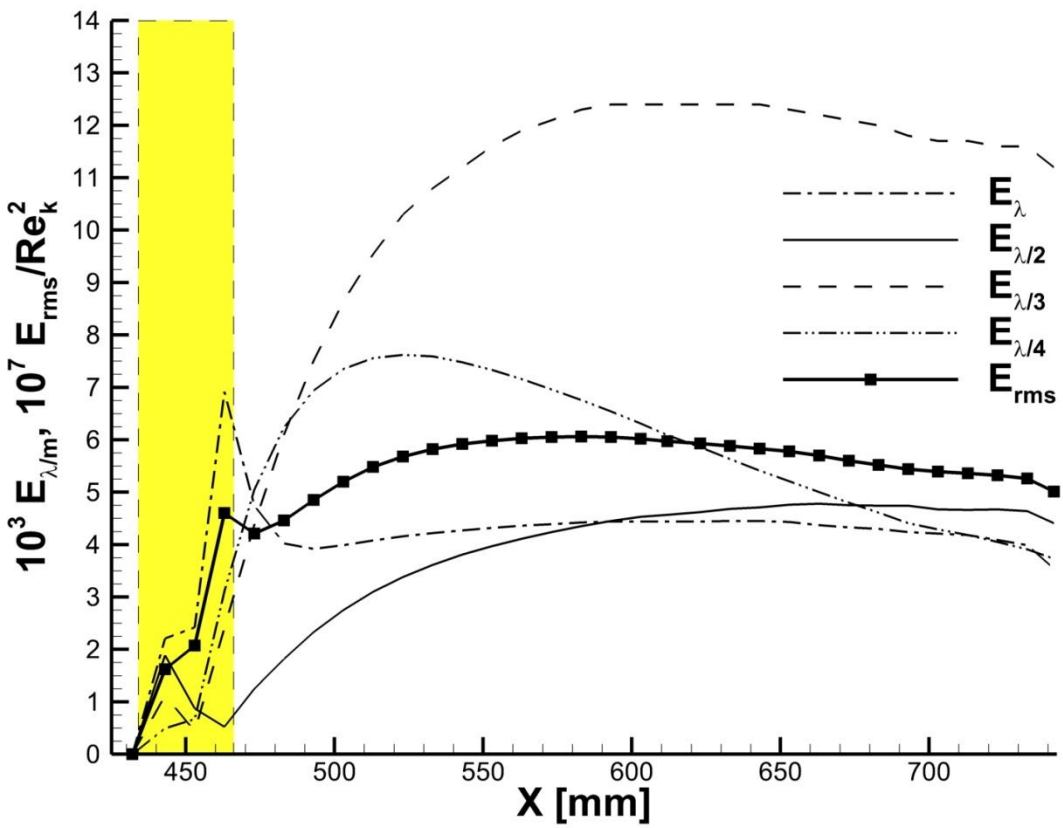

Figure 39: Disturbance energies for the *λ-λ/4* wavelengths and rms for the "tall roughness only" geometry. Note: different y axis scales for E_λ and E_{rms}, as well as different y axis range than in previous disturbance energy figures.

Better understanding of how the differences in geometries correlate to differences in the disturbance energies is crucial for understanding laminar flows over roughness. A comparison of rms disturbance energies is shown in figure 40. The rms disturbance

energies for the full roughness and slip surface geometries are very similar, almost falling directly on top of one another. The "tall roughness only" geometry shows a similar shape to those two, but at a higher value.

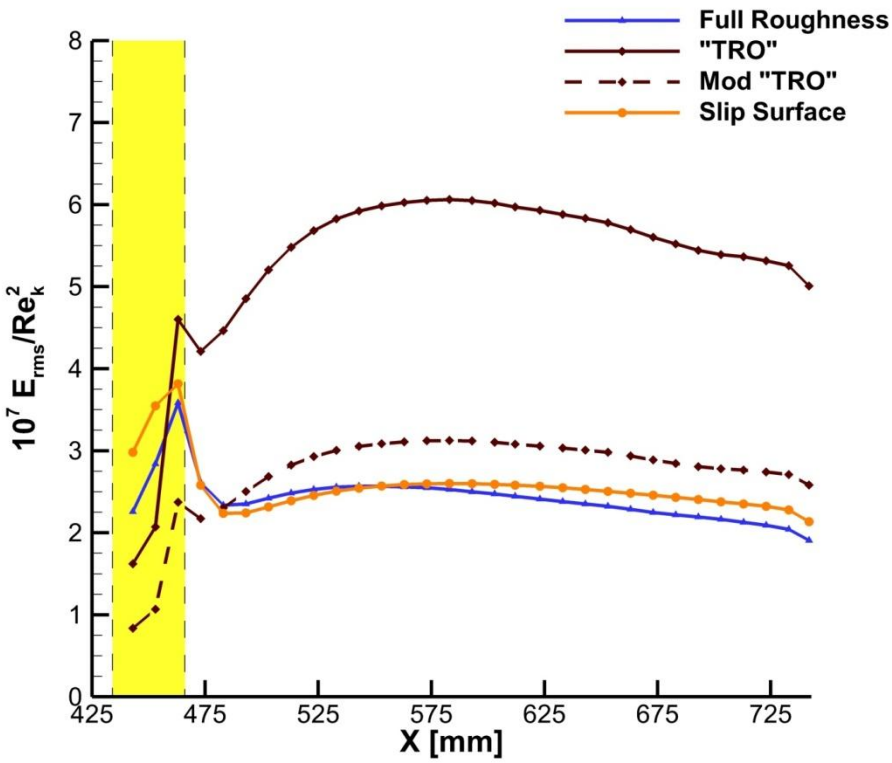

Figure 40: Comparison of rms disturbance energy at an Re_k of 227 for the full roughness, slip surface, and "tall roughness only" geometries. Dashed orange line represents modified results for the full roughness geometry.

An examination of figure 40 suggests that rescaling E_{rms} with a different height ,k, for the "tall roughness only" geometry may lead to better agreement with the full roughness geometry and thus aid one's understanding of the effect of the small scale roughness on the rms energy. Determining what the scale factor should be, however, is not such a trivial task. The scaling used in figure 40 is based on the average height of the

positive amplitudes in the full roughness geometry, 0.28 mm. This is used to change the height associated with the Re_k calculation, resulting in a new Re_k for the "tall roughness only" geometry of 291. The result of this new Re_k is shown as the dashed brown line in figure 40. Because the y axis is scaled by $1/Re_k^2$, a higher Re_k lowers the peak value of E_{rms}. Although this simple scaling does not lead to prefect agreement, it does indicate an important result. The smaller scale roughness surrounding the tallest regions of roughness provides some sort of "Re_k relief" in which the incoming flow approaching the tallest elements behaves as if it is at a lower Re_k than it actually is. The very small scale roughness displaces incoming flow upward so that the effective height, k, of the tallest elements protruding into the laminar boundary layer is reduced. However, the deep valleys which contain separated flow do not effectively raise the height of the tallest elements since the flow separates. Exactly how much "Re_k relief" is present is yet to be determined and is not simply the average height of the full roughness geometry.

B. Re_k 227 Superposition of Tallest Regions of Roughness

Further analysis of the Re_k 227 "tall roughness only" geometry is performed to determine if the three isolated regions of roughness together act as a linear superposition of the individual regions run separately. The three individual roughness geometries ("A", "B", and "C") correspond to the tall regions of roughness at A, B, and C presented previously and are shown next to the "tall roughness only" geometry in figure 41. (Note: a fourth geometry consisting of only the non-positive amplitudes, "valleys", is also simulated. Results show negligible effects on the flow and are thus not presented. This indicates that the "valleys" do not contribute to the near-field detatils).

To determine if the "tall roughness only" case is indeed a linear superposition of the individual roughness geometries, ω_x slices are taken for each of the individual roughness geometries 475 mm downstream of the flat plate leading edge. Each individual contribution of ω_x is shown in its respective location for the individual roughness geometries and compared against the "tall roughness only" geometry in figure 42. The center images, corresponding to the roughness at z/λ_k=-0.05, are almost identical; the z/λ_k=-0.05 roughness in the "tall roughness only" geometry creates very similar flow structures to those created by the "B" geometry individually. Also, the right images, corresponding to the roughness at z/λ_k=0.2, create nearly identically shaped vortical structures with only a slight difference in magnitude. The streamwise vorticity for the "tall roughness only" geometry is about 5-10% stronger than for the "C" geometry run individually. This indicates that there is a good degree of linear independence in the "tall roughness only" geometry.

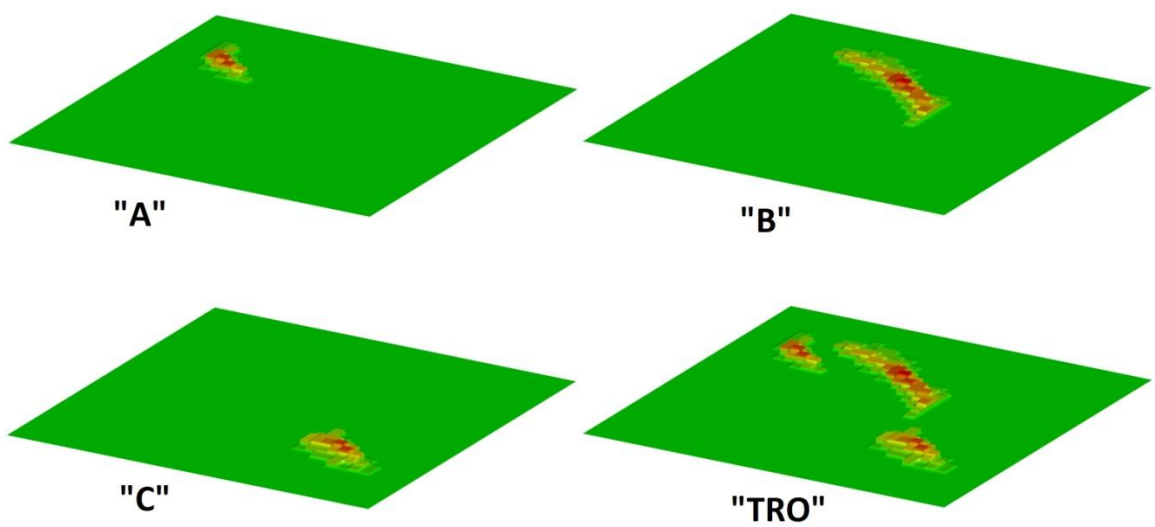

Figure 41: "A", "B", and "C" geometries. "Tall roughness only" geometry shown as comparison. Addition of the three individual roughness geometries yields "tall roughness only" geometry.

The middle and right regions of roughness create nearly identical near-field structures when run either together or separately. However, some differences are found when examining the left region of roughness at z/λ_k=-0.3. In the case of the "tall roughness only" geometry, the left region of roughness creates a pair of counter rotating vortices similar to those seen in flow past a symmetric roughness element such as a cylinder. When the "A" geometry is run by itself, it creates a single asymmetric vortex core, even though the velocity deficit region created by this single vortex is fairly symmetric. It is clear that the "B" and "C" regions of roughness have an effect on the flow around the "A" region of roughness and the three regions of roughness are not completely independent.

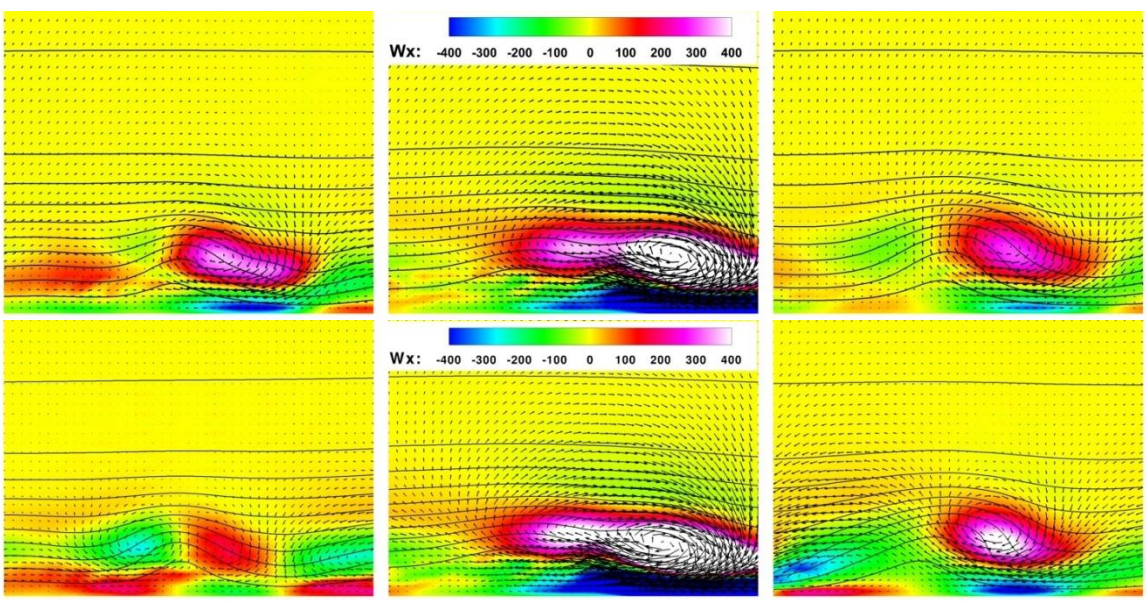

Figure 42: 475 mm downstream slices corresponding to regions of roughness at z=6, 14, and 23 mm, respectively. Top images are for the individual "A", "C", and "B" geometries and bottom images are for the "tall roughness only" geometry. Contour lines are in 10% U_∞ increments and colors are ω_x.

To determine the extent to which the influences of the individual "A", "B", and "C" geometries linearly add, the spanwise domain is broken down into three distinct zones. The first zone spans from z/λ_k=-0.5 to z/λ_k=-0.19. This zone encompasses the wake of the "A" geometry. The second and third zones span from z/λ_k=-0.188 to z/λ_k=0.16 and z/λ_k=0.16 to z/λ_k=0.5, respectively. These two zones encompass the wakes of the "B" and "C" geometries. The three distinct zones are stitched together to create hybrid domain to compare U velocity contours and rms disturbance velocity profiles against the "tall roughness only" geometry. At z/λ_k=-.188 and z/λ_k=0.16, the data are averaged between the two adjacent zones to create a smoother transition, however discontinuities still appear in the contour lines. Figures 43 and 44 show the U velocity contours and root mean square velocity profiles, respectively, for the hybrid domain and "tall roughness only" simulation.

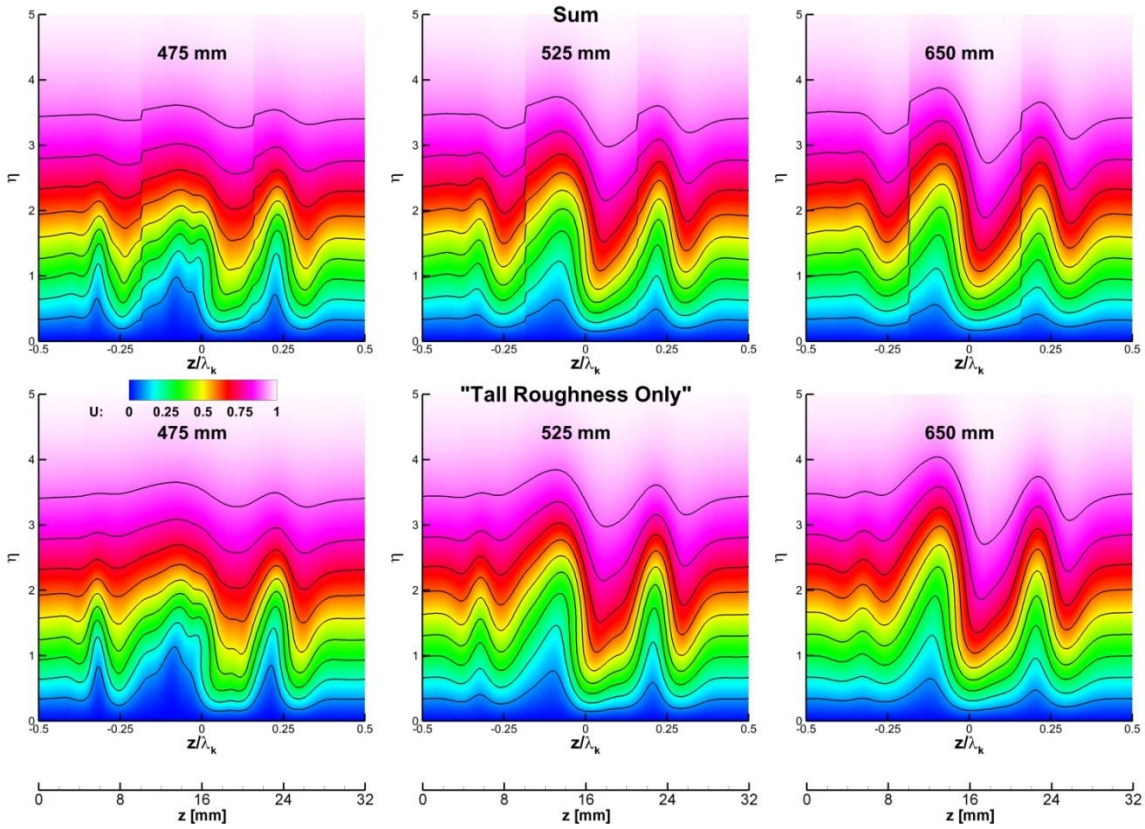

Figure 43: Comparison of streamwise velocity contours for the "A", "B", and "C" individual geometries hybrid sum and "tall roughness only" geometry. Discontinuities in top image occur at interface between the zones described earlier. Contour lines are in 10% U_∞ increments and colors are U.

The contours in figure 43 show nearly identical results at all downstream locations. The middle velocity deficit region, centered around z/λ_k=-0.05, has the same shape in both data sets, including the small dip occurring near z/λ_k=-0.05. As the flow continues downstream, the dip disappears to create the far-field wake details. The right velocity deficit region, centered around z/λ_k =0.23, shows an excellent agreement between the two data sets as well. Differences start to appear in the left velocity deficit region, centered around z/λ_k =-0.3, in the 525 and 600 mm downstream slices. At 475 mm, both the "tall roughness only" and sum results show a symmetric peak to indicate a

pair of counter rotating vortices. However, figure 42 shows a single asymmetric vortex for the "A" geometry as opposed to a counter rotating pair for the "tall roughness only" geometry. At 525 mm and further downstream, the left velocity deficit region shows an asymmetric peak associated with the single asymmetric vortex present.

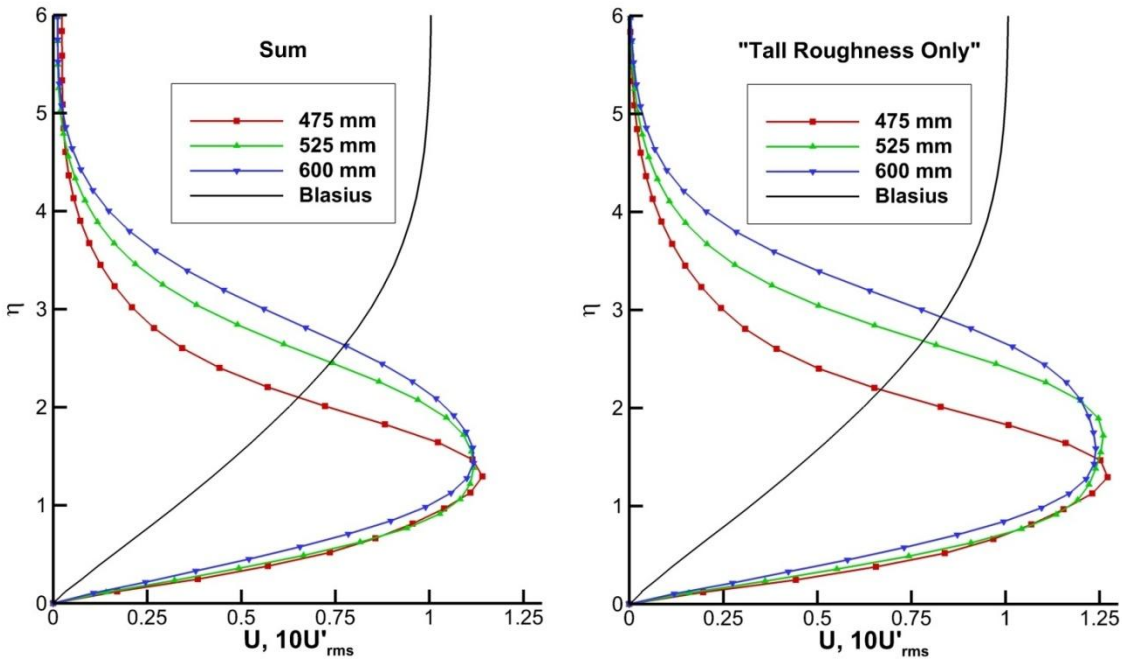

Figure 44: RMS disturbance velocity profiles for the hybrid sum and "tall roughness only" geometries. Note: different x axis scales for U and U'_{rms}.

The "sum" results presented on the left image of figure 44 are computed as simply the sum of the "A", "B", and "C" rms disturbance velocity profiles and show good agreement to the "tall roughness only" geometry. (Note: the differences in disturbance velocity profiles and thus the disturbance energies are negligible when the quantities are calculated as previously described or calculated from the stitched domain results shown in figure 43). Although the peak magnitudes of U'_{rms} differ by about 10%, both data sets show qualitatively similar trends. As the flow moves downstream, the disturbances themselves move higher up in the boundary layer, as is seen in previous geometries and

Re_k values. The main difference between these and previously presented results is the lack of a decrease in peak magnitude at progressively further downstream locations. The disturbances created as the flow moves past the roughness geometry appear stable; no transition to turbulence occurs at an Re_k of 227, but disturbances do not dissipate as the flow continues downstream. This result is seen in both the "tall roughness only" results presented earlier and in the hybrid sum of the "A", "B", and "C" geometries currently being discussed.

Finally, a comparison between the rms disturbance energies for the individual ("A", "B", and "C") geometries, their "sum" (computed as the sum of the "A", "B", and "C" rms disturbance energies), and the "tall roughness only" geometry is performed and presented in figure 45. As suggested by the size of the velocity deficit region in figure 42, the "B" geometry creates the largest disturbance energy profile with an overall shape similar to that of the "tall roughness only" geometry. The "A" geometry shows a flat profile throughout the entire streamwise domain and the "C" geometry shows a higher initial value of disturbance energy before dissipating to the same value as the "A" geometry by the end of the domain. Adding these three profiles creates the "sum" profile. The "sum" profile lies somewhat under the "tall roughness only" profile but otherwise has a very similar shape. This indicates that the individual roughness region geometries add to create a very similar disturbances (also seen previously in figure 44) to the "tall roughness only" geometry, albeit at a lower magnitude.

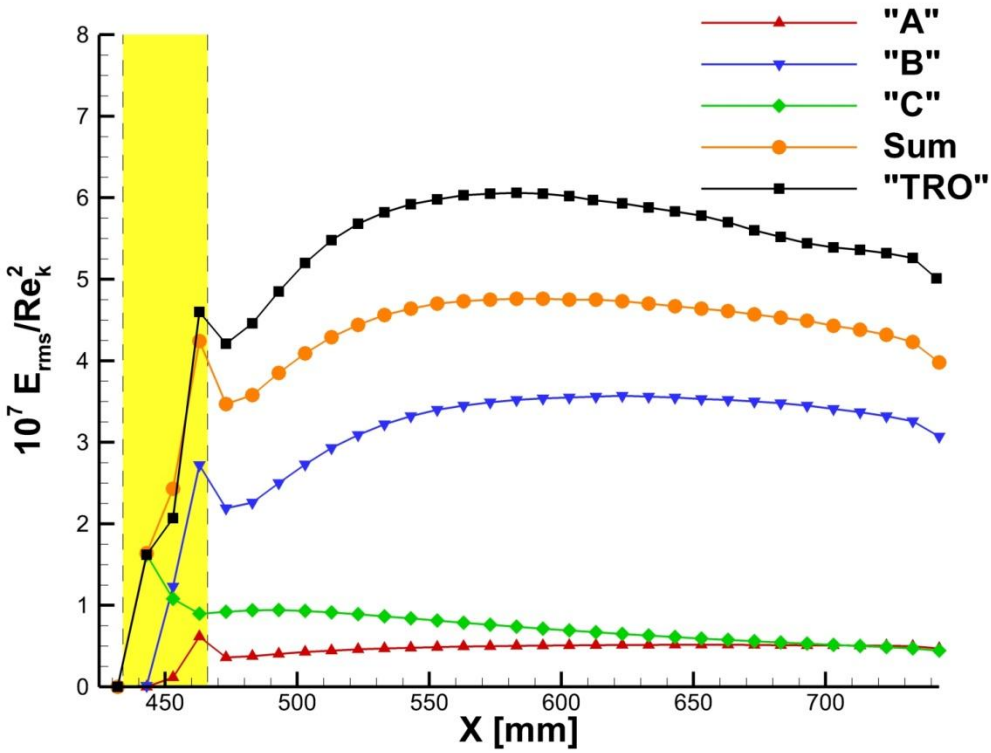

Figure 45: RMS disturbance energy profiles for "A", "B", and "C" geometries, their sum, and "tall roughness only" geometry.

Further breakdown of the "sum" and "tall roughness only" disturbance energy profiles is performed to determine the additive nature of the individual wavelength components to the root mean square. Figure 46 shows the individual wavelength components of the disturbance energy for λ, $\lambda/2$, $\lambda/3$, and $\lambda/4$, respectively. The top left image of figure 46 shows the E_λ profiles for the "sum" and "no valleys." Both profiles reach the same peak magnitude over the roughness patch before diverging from one another at further downstream. The "sum" profile shows relatively constant linear growth throughout the domain unlike the flat profile of the "tall roughness only" simulation. Despite the difference in downstream energy growth, both E_λ profiles are quite close. The $E_{\lambda/2}$, $E_{\lambda/3}$, and $E_{\lambda/4}$ profiles shown in top right, bottom left, and bottom

right images of figure 46 do not show similar energy levels between the "sum" and "tall roughness only", but rather similar overall shapes. The *λ/2* wavelength undergoes more excitation in the sum than the "tall roughness only" case because the "B" individual geometry spans approximately half the spanwise domain, leading to large excitation. The interaction of the left and right regions of tallest roughness in the "tall roughness only" simulation decreases this excitation, instead leading to larger excitation of the *λ/3* and *λ/4* wavelengths.

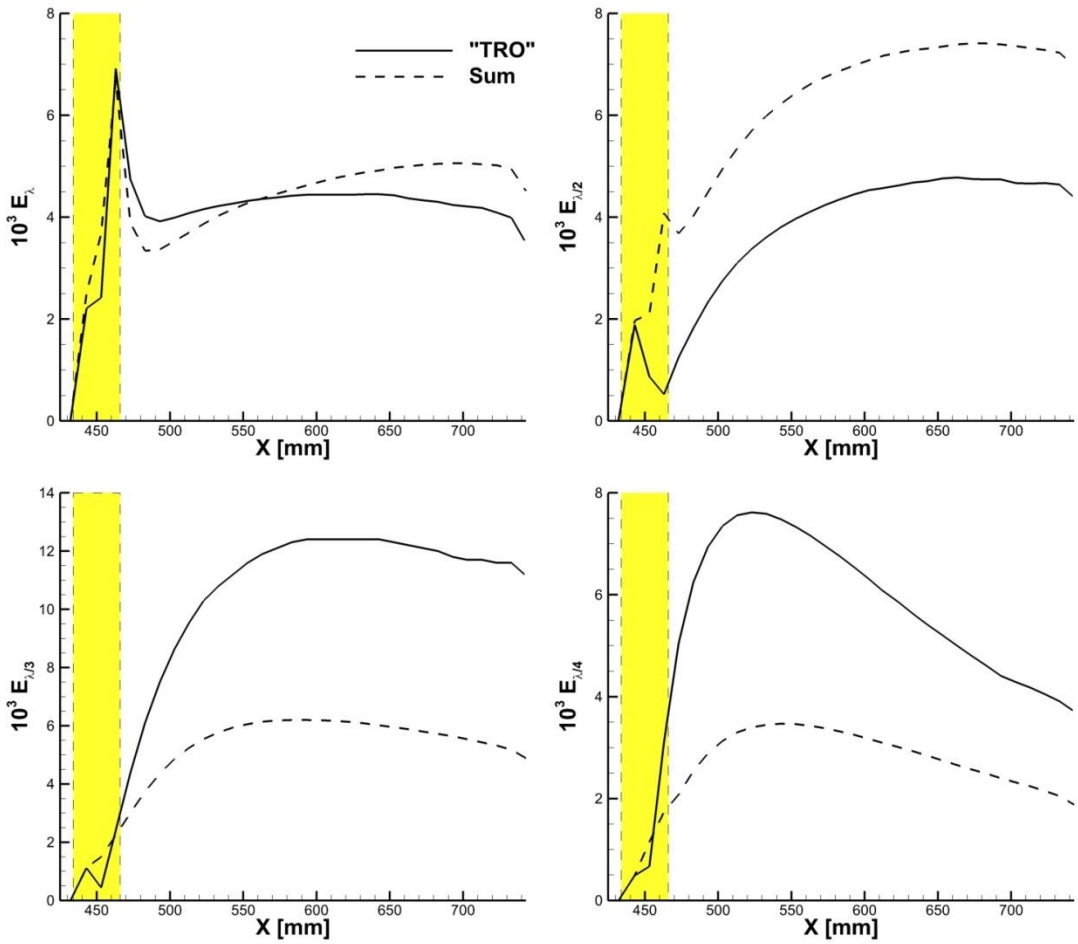

Figure 46: Individual wavelength disturbance energies for the "A", "B", and "C" sum and "tall roughness only" geometries. Top left image is E_λ profiles, top right is $E_{\lambda/2}$, bottom left is $E_{\lambda/3}$, and bottom right is $E_{\lambda/4}$.

Breaking down the "tall roughness only" geometry into its individual components yields similar qualitative results, however some discrepancies exist with quantitative results. Examining the qualitative results (figures 42 and 43) of the velocity deficit regions and vorticity contours, one can prematurely conclude that the individual "A", "B", and "C" result can be linearly superposed to recreate the "tall roughness only" results with little error. However, comparing the detailed quantitative results, rms disturbance velocity profiles, rms disturbance energies, and individual mode disturbance energies (figures 44-46), indicates the superposition of the individual geometries somewhat under predicts the actual results of the "tall roughness only" geometry. Thus the non-linear interaction of the three tallest regions of roughness in the "tall roughness only" geometry must be considered when examining the flows.

VI. CONCLUSION

Direct numerical simulation is used to model the near-field of flow past roughness elements. Two types of roughness are investigated, cylinders and quasi-random distributed roughness. The cylinders are modeled to match hotwire experiments, water channel LDA measurements, and alternate DNS with an Re_k of 202 and spanwise periodicity of $d/\lambda = 1/3$.[3,4,5,6] Prior simulations showed discrepancies with experiments. The quasi-random distributed roughness simulated matched the experimental roughness at Re_k values of 164, 227, and 301.[7] The focus of the current work was on resolving the discrepancies of earlier isolated cylindrical roughness element results and investigating the effect of more realistic roughness on near-field details and transition.

To address the differing results for the cylinders, a higher resolution grid is used (2x spanwise resolution and 2x streamwise resolution) than in previous simulations.[6] The increase in resolution removes the three hump wake profile and produces excellent agreement with experiments (both hotwire and LDA) and alternate DNS.[3] Flow visualization performed in the water channel agrees with DNS findings of there being three collar vortices as opposed to the two seen in alternate DNS.[3]

Results for the quasi-random distributed roughness show good agreement with experiments.[7] For all three values of Re_k examined, three distinct velocity deficit regions are present. These velocity deficit regions are created as streamwise vorticity, ω_x, pulls lower velocity flow from near the wall up into the boundary layer. The vorticity exists as either a pair of counter rotating vortices or a single asymmetric vortex depending on the shape of a particularly tall roughness upstream. For the Re_k 164 and 227 simulations, this vorticity creates stable disturbances that do not cause a transition to turbulence. For the Re_k 301 simulation, the disturbances are stronger, creating a transition to turbulence

between 625 and 700 mm downstream of the flat plate leading edge, also seen in experiments. Determination of the transition point is obtained by both a calculation of the disturbance energy and visualization of λ_2.

Further investigation is performed at an Re_k of 227 to determine the effect of individual components of the full roughness geometry on the near-field. The non-positive amplitudes are first replaced with a streamwise and spanwise slip surface at the flat plate height. Results are nearly identical to those with the full roughness geometry indicating the "valleys" main function is to allow non-zero velocity at flat plate height. The full roughness geometry is further decomposed into only the three regions of tallest roughness. Results show the same three velocity deficit region shapes but at a higher magnitude due to the more pronounced disturbances of isolated roughness elements. The larger disturbances occur due to the lack of small scale roughness upstream of these three tallest regions. Disturbance energy profiles show removal of the small scale peripheral roughness results in larger magnitudes than for the full roughness geometry. We infer that the small scale roughness causes the flow over the largest roughness elements to behave as though it is at a lower Re_k.

Linear superposition of the three individual regions of tallest roughness is also examined. Qualitative results for the near-field flow structures show good agreement between the sum of the three regions of tallest roughness and the "tall roughness only" geometry. However, quantitative analysis shows discrepancies in both rms disturbance velocity profiles and disturbance energies; the sum of the three tallest regions of roughness under predicts both of these quantities. A simple addition of individual components of the full roughness geometry is not quite sufficient to recreate the full roughness geometry because non-linear interaction exists between the individual components.

VII. FUTURE WORK

In the future, a few discrepancies should be addressed. The first deals with creating a smoother representation of the simulated roughness to better recreate the actual machined roughness of Downs et al.[7] Removal of the sharp corners and stairsteps present in the current simulated roughness may remove the stronger gradients present in the simulations and provide better agreement with experiments. A second improvement would be to remove the slight adverse pressure gradient in the incoming Blasius flow. This may also help to lessen the gradients present in the simulations. Incorporating both changes into the DNS should help in recreating the experiments[7] as closely as possible.

A further investigation into the turbulent nature of the Re_k 301 simulation may provide insight into the breakdown of the initial disturbances into full turbulence. This will entail the use of both a larger domain in the streamwise direction and longer run times. With the new results, not only will one be able to visualize the intermittent turbulence seen near 625-700 mm downstream of the flat plate leading edge but also examine a fully turbulent flow at some location beyond the 744 mm downstream location where the domain used in current simulations ends.

REFERENCES

[1]Reshotko, E., "Transient Growth—A Factor in Bypass Transition." *Physics of Fluids*, Vol. 13, No. 5, May 2001, pp. 1067–1075.

[2]Reshotko, E., and Tumin, A., "Role of Transient Growth in Roughness-Induced Transition," *AIAA Journal*, Vol. 42, No. 4, Apr 2004, pp. 766-770.

[3]Rizzetta, D. P. and Visbal, M. R., "Direct Numerical Simulations of Flow Past an Array of Distributed Roughness Elements," *AIAA Journal*, Vol. 45, No. 8, Aug. 2007, pp. 1967-1976.

[4]Ergin, F. G. and White, E. B., "Unsteady and Transitional Flows Behind Roughness Elements," *AIAA Journal*, Vol. 44, No. 11, Nov. 2006, pp. 2504-2514.

[5]Stephani, K. A. and Goldstein, D. B., "DNS Study of Transient Disturbance Growth and Bypass Transition Due to Realistic Roughness," 47th AIAA Aerospace Sciences Meeting, American Institute of Aeronautics and Astronautics, Orlando, FL, 2009.

[6]Doolittle, C. J., "Near-Field Flow Structures and Transient Growth Due to Subcritical Surface Roughness," Masters Thesis, University of Texas at Austin, Austin, TX, 2010.

[7]Downs, R. S., White, E. B., and Denissen, N. A., "Transient Growth and Transition Induced by Random Distributed Roughness," *AIAA Journal*, Vol. 46, No. 2, Feb. 2008, pp. 451-462.

[8]White, E. B., "Transient Growth of Stationary Disturbances in a Flat Plate Boundary Layer," *Physics of Fluids*, Vol. 14, No. 12, Dec. 2002, pp. 4429-4439.

[9]Andersson, P., Berggren, M., and Henningson, D. S., "Optimal Disturbances and Bypass Transition in Boundary Layers," *Physics of Fluids*, Vol. 11, No. 1, Jan. 1999, pp. 134-150.

[10]Tumin, A., and Reshotko, E., "Spatial Theory of Optimal Disturbances in Boundary Layers," *Physics of Fluids*, Vol. 13, No. 7, Jul. 2001, pp. 2097-2104.

[11]White, E. B., "Transient Growth of Stationary Disturbances in a Flat Plate Boundary Layer," *Physics of Fluids*, Vol. 14, No. 12, Dec. 2002, pp. 4429-4439.

[12]Nikuradse, J., "Laws of Flow in Rough Pipes," NACA Technical Memorandum 1292, July/August, 1933.

[13]von Doenhoff, A. E. and Elmer, A. H., "A Low Speed Experimental Investigation of the Effect of a Sandpaper Type Roughness on Boundary-Layer Transition," NACA Report 1349, Aug. 1956.

[14]Dassler, P., Kožulović, D., and Fiala, A., "Modelling of Roughness-Induced Transition Using Local Variables," European Conference on Computational Fluid Dynamics, Lisbon, Portugal, 2010.

[15]Goldstein, D. B., Handler, R., and Sirovich, L., "Modeling a No-Slip Flow Boundary with an External Force Field," *Journal of Computational Physics*, Vol. 177, Apr. 1993, pp. 354-366.

[16]Handler, R. A., Hendricks, E. W., and Leighton, R. I., "Low Reynolds Number Calculation of Turbulent Channel Flow: A General Discussion," NRL Memorandum Report 6410, 1989, pp. 1-103.

[17]Kim, J., Moin, P., and Moser, R., "Turbulence Statistics in Fully Developed Channel Flow at Low Reynolds Number," *Journal of Fluid Mechanics*, Vol. 177, Apr 1987, pp. 133-166.

[18]Moin, P. and Kim, J., "Numerical Investigation of Turbulent Channel Flow," *Journal of Fluid Mechanics*, Vol. 118, May 1982, pp. 341-377.

[19]Strand, J. S., "DNS of Surface Textures to Control Growth of Turbulent Spots," Masters Thesis, University of Texas at Austin, Austin, TX, 2007.

[20]Saric, W. S., "Low-Speed Boundary Layer Transition Experiments," *Transition: Experiments, Theory and Computation*, edited by T. C. Corke, G. Erlebacher, and M. Hussaini, Oxford Univ. Press, Oxford, 1996, pp. 1-114.

[21]Doolittle, C., Drews, S., and Goldstein, D., "Near-field flow structures about subcritical surface roughness," Submitted to AIAA Journal.

[22]Jeong, J. and Hussain, F., "On the Identification of a Vortex," *Journal of Fluid Mechanics*, Vol. 285, 1995, pp. 69-94.

VITA

Scott was born in Sarasota, Florida on March 8, 1987 to Mike and Kathy Drews. He grew up in Sarasota before moving to Jacksonville, Florida to attend high school at The Bolles School. After which, Scott attended the University of Texas at Austin until December of 2009 when he graduated with a Bachelor of Science degree in Aerospace Engineering. Scott continued his education at the University of Texas at Austin, researching fluid dynamics under the direction of Dr. David Goldstein.

Email: scottdrews@utexas.edu

This thesis was typed by the author.